



## Preparation of size-controlled silver phosphate catalysts and their enhanced photocatalysis performance via synergistic effect with MWCNTs and PANI

Yan Lin<sup>a</sup>, Shaohua Wu<sup>a</sup>, Chunping Yang<sup>a,b,\*</sup>, Ming Chen<sup>a,\*</sup>, Xiang Li<sup>a</sup>



<sup>a</sup> College of Environmental Science and Engineering, Hunan University and Key Laboratory of Environmental Biology and Pollution Control (Hunan University), Ministry of Education, Changsha, Hunan 410082, China

<sup>b</sup> Guangdong Provincial Key Laboratory of Petrochemical Pollution Process and Control, School of Environmental Science and Engineering, Guangdong University of Petrochemical Technology, Maoming, Guangdong 525000, China

### ARTICLE INFO

**Keywords:**  
MWCNTs  
PANI  
Photocatalysis  
Size-controlled  
Visible light catalyst

### ABSTRACT

In this work, novel photocatalysts  $\text{Ag}_3\text{PO}_4@\text{MWCNTs@PANI}$  with excellent visible light photocatalytic performance and photostability were successfully prepared by a facile in-situ precipitation method. The optimal catalyst  $\text{Ag}_3\text{PO}_4@0.1\%\text{MWCNTs}@3\%\text{PANI}$  showed the highest photocatalytic performance for degradation of phenol and p-nitrophenol, the apparent rate constant of which was 21.9 and 10 times than that of the pure  $\text{Ag}_3\text{PO}_4$ , respectively. Interestingly, the  $\text{Ag}_3\text{PO}_4$  exhibited significant changes in particle size, which changed from 10 to 20  $\mu\text{m}$  for pure  $\text{Ag}_3\text{PO}_4$  particles into 0.38–1.0  $\mu\text{m}$  and 0.15–0.38  $\mu\text{m}$  with the addition of MWCNTs and PANI, respectively. In presence of MWCNTs, similar phenomena have been reported in our previous studies, while the ability of PANI dissolved in the presence of DMF solvent to control the size of  $\text{Ag}_3\text{PO}_4$  crystal was reported for the first time. The dramatic enhancement of photocatalytic activity and photostability could be attributed to the synergistic effect between MWCNTs and PANI on  $\text{Ag}_3\text{PO}_4$ . The MWCNTs penetrating in the bulk phase of  $\text{Ag}_3\text{PO}_4$  could serve as conductors of photogenerated electrons and rapidly migrated electrons to the surface of the photocatalysts. Meanwhile, photogenerated holes in the valence band of  $\text{Ag}_3\text{PO}_4$  were transferred to the photocatalysts surface through HOMO of PANI. Consequently, high separation efficiency of electron-hole pairs was successfully achieved. A novel design and preparation strategy for photocatalyst was proposed to simultaneously achieve the small size control of catalyst crystal and improve the photocatalytic performance of catalyst by adding MWCNT and PANI.

### 1. Introduction

In recent decades, photocatalysis has attracted much attention because of its direct utilization of solar energy and became one of the most promising technologies in environmental remediation [1,2]. Nevertheless, unsatisfactory photocatalytic activity of most semiconductor photocatalysts in visible light region is still hampering its wide application. Investigations and development of efficient visible light driven photocatalyst is thus the key to solving this technology bottleneck. Silver phosphate ( $\text{Ag}_3\text{PO}_4$ ) has been reported for its excellent photocatalytic degradation of organic pollutants under visible light, which can achieve the quantum efficiency of up to 90% in the visible region [3]. Moreover, a lot of research has been carried out to systematically study the photocatalytic performance of  $\text{Ag}_3\text{PO}_4$ , and confirmed that  $\text{Ag}_3\text{PO}_4$  could obviously show better photocatalytic activity than many other visible light driven catalysts [3–6]. This might be attributed to the

fact that photogenerated holes in the valence band of  $\text{Ag}_3\text{PO}_4$  possessed very strong oxidative ability and could directly oxidize and degrade the pollutants efficiently.

Unfortunately,  $\text{Ag}_3\text{PO}_4$  has a relatively severe photocorrosion, and the photocatalytic activity of  $\text{Ag}_3\text{PO}_4$  is also closely related to its size and morphology, which hinders its wide applications. For example, Bi et al. found that  $\text{Ag}_3\text{PO}_4$  rhombic dodecahedrons exhibited much higher catalytic activities than  $\text{Ag}_3\text{PO}_4$  cubes for the degradation of organic contaminants under visible-light irradiation [3]. Yang et al. also reported that  $\text{Ag}_3\text{PO}_4$  polyhedra with an average diameter of more than 15  $\mu\text{m}$  showed much less photocatalytic activity than sphere-like polyhedral morphology with an average diameter of 450 nm [7,8]. So the shortcomings that  $\text{Ag}_3\text{PO}_4$  samples tend to form big size and irregular polyhedral microstructures during the preparation should be overcome. As for the photocorrosion, it could be attributed to the low migration and separation efficiency of photogenerated electron-hole pairs. If the

\* Corresponding authors at: College of Environmental Science and Engineering, Hunan University and Key Laboratory of Environmental Biology and Pollution Control (Hunan University), Ministry of Education, Changsha, Hunan 410082, China.

E-mail addresses: [yangc@hnu.edu.cn](mailto:yangc@hnu.edu.cn) (C. Yang), [mchensn@hnu.edu.cn](mailto:mchensn@hnu.edu.cn) (M. Chen).

photoproduced carriers generated by  $\text{Ag}_3\text{PO}_4$  could not be rapidly migrated to other materials or pollutants, the  $\text{Ag}^+$  can be easily reduced into metal Ag by excited electrons, and photogenerated holes also oxidize  $\text{Ag}_3\text{PO}_4$  itself [4,9].

Enormous efforts have been devoted to overcoming the above-mentioned drawbacks, such as combining  $\text{Ag}_3\text{PO}_4$  with another semiconductor [10,11], or adding other materials to form hybrid photocatalysts [7,12], or improving synthesis procedures [3,13]. Multi-walled carbon nanotubes (MWCNTs) are one of promising carbon-based nanomaterials with very high aspect ratio, excellent electrical conductivity, good mechanical properties, and favorable transmission features [14,15]. Because of its unique properties, the combination of MWCNTs with other semiconductors to improve the photocatalytic activity has been reported [16,17]. For instance, due to the good conductivity of MWCNTs, the electrons in the CB of  $\text{WO}_3$  and  $\text{Ag}_3\text{PO}_4$  could be easily transferred to the surface of MWCNTs to participate in the photocatalytic reaction [17]. In our previous work, we have demonstrated that the introduction of MWCNTs could obviously changed the size and morphology of  $\text{Ag}_3\text{PO}_4$ , which transformed from a polyhedron with a diameter of about 30  $\mu\text{m}$  into a spherical-like crystal with a diameter of 0.28–0.69  $\mu\text{m}$ . Meanwhile, the presence of MWCNTs could also enhance the photocatalytic activity and inhibit the photocorrosion of  $\text{Ag}_3\text{PO}_4$  remarkably [8]. The present work explored further about this topic and employed longer MWCNTs with a length of 10–30  $\mu\text{m}$ , which have the potential to provide more adsorption sites for  $\text{Ag}^+$  and exhibits better bonding ability with  $\text{Ag}_3\text{PO}_4$  crystal. On the above basis, this study focused on combining  $\text{Ag}_3\text{PO}_4@\text{MWCNTs}$  with other materials to further improve its photocatalytic performance and overcome the problems of photocorrosion and big crystal size of  $\text{Ag}_3\text{PO}_4$ .

Conductive polyaniline (PANI) is a kind of  $\pi$ -conjugated long chain polymer, which consists of benzenoid and quinonoid units with the delocalized conjugated structures [18]. Moreover, PANI has raised widespread concern due to its advantages of high conductivity, good environment stability, low cost and convenient production [19]. Recently, some studies have focused on the combination of PANI and semiconductor to improve the photocatalytic performance and photostability of the photocatalyst. For example, after hybridization with PANI, the photocatalytic activity of carbon nitride nanosheets [20],  $\text{TiO}_2$  [18],  $\text{CdS}$  [21] and  $\text{ZnO}$  [22] were all enhanced remarkably. Zhang et.al found that photogenerated holes in the VB of CdS can be transferred to the photocatalysts surface through HOMO of PANI [21]. The holes in VB of  $\text{TiO}_2$  can directly transfer to HOMO of PANI, and the photogenerated holes can emigrate to the photocatalysts surface easily [18]. And photogenerated holes in the ZnO valence band also could transfer to the HOMO orbital of PANI and then emigrate to the photocatalysts surface and oxidize the adsorbed contaminants directly [23]. These successful cases demonstrated that PANI has the unique strong photogenerated holes trapping and transporting properties, which could increase the holes migration rate, improve the separation of carriers, and consequently enhance photocatalytic activity of the photocatalysts. Therefore, considering the unique properties of MWCNTs and PANI, MWCNTs were utilized as the photogenerated electron conductors and PANI as the hole-transporting material. It is expected to further improve the separation efficiency of carriers, and thus enhance the photocatalytic performance and anti-photocorrosion of  $\text{Ag}_3\text{PO}_4$ .

However, there were no reports about the novel photocatalyst of  $\text{Ag}_3\text{PO}_4@\text{MWCNTs@PANI}$ , which combines the advantages of PANI and MWCNTs and should have the potential of excellent visible-light-driven photocatalytic performance and photostability. Moreover, data and reports on the investigations of notable changes in size and morphology of  $\text{Ag}_3\text{PO}_4$  crystals caused by PANI are not available. Therefore, in present work, novel  $\text{Ag}_3\text{PO}_4@\text{MWCNTs@PANI}$  composite photocatalyst was firstly prepared by a facile in-situ precipitation method. Its micro-morphology structures, chemical compositions, photocatalytic activities and photostability were fully characterized and

discussed. Phenol and p-nitrophenol were chosen as the target pollutants to evaluate photocatalytic performance of the photocatalysts, and its mineralization ability were measured by TOC and 3D EEMs technologies. Taking the practical application into consideration, the effects of pH and coexisting ions were also investigated. The photodegradation mechanisms were explored using ESR and radical trapping experiments. This study proposed a new scheme to design novel silver phosphate-based photocatalysts with great potential to alleviate severe energy crisis and environmental pollution nowadays.

## 2. Experimental

### 2.1. Chemicals

Silver nitrate ( $\text{AgNO}_3$ ), Disodium hydrogen phosphate dodecahydrate ( $\text{Na}_2\text{HPO}_4 \cdot 12\text{H}_2\text{O}$ ), ethanol ( $\text{CH}_3\text{CH}_2\text{OH}$ ), *N,N*-Dimethylformamide (DMF), phenol and P-nitrophenol (PNP) were purchased from Sinopharm Chemical Reagent Co., Ltd. (Shanghai, China). Polyaniline (PANI > 98%) was purchased from Bide Pharmatech Ltd. (Shanghai, China). All the reagents were of analytical grade, and de-ionized water (18.25  $\Omega\text{cm}$ ) was used in the whole experiment. Multi-walled carbon nanotubes (MWCNTs > 95%, Hydroxyl content: 3.06 wt%) with a mean outer diameter of 10–20 nm and length of 20–30  $\mu\text{m}$  were purchased from Nanjing Xianfeng Nano Materials Technology Co., Ltd. (Nanjing, China). MWCNTs were purified according to our method reported previously [8].

### 2.2. Preparation of $\text{Ag}_3\text{PO}_4$ , $\text{Ag}_3\text{PO}_4@\text{MWCNTs}$ and $\text{Ag}_3\text{PO}_4@\text{PANI}$

The synthetic method of  $\text{Ag}_3\text{PO}_4@\text{MWCNTs}$  was referred to our previously reported methods [8]. Firstly, a certain amount of MWCNTs was dispersed into de-ionized water (30 mL) via sonication for 3 h. Secondly, 30 mL of 18 mmol  $\text{AgNO}_3$  aqueous solution was added to the above MWCNTs aqueous suspension and then stirred violently in dark for 12 h. Afterwards, 30 mL of  $\text{Na}_2\text{HPO}_4 \cdot 12\text{H}_2\text{O}$  aqueous solution (6 mmol) was added dropwise to the mixture with 6-hour constant stir in a dark condition. Finally, the obtained precipitate was washed with de-ionized water for several times, and dried in vacuum (60°C) overnight. For comparison, pure  $\text{Ag}_3\text{PO}_4$  was also prepared under conditions identical to those of  $\text{Ag}_3\text{PO}_4@\text{MWCNTs}$  in the absence of MWCNTs.

Although the PANI is hardly soluble in water, it can be dissolved and dispersed well in DMF [23], DMF was thus introduced in the preparation process. The preparation procedure of  $\text{Ag}_3\text{PO}_4@\text{PANI}$  was as follows. Firstly, a certain amount of PANI was dispersed into 30 mL of *N,N*-Dimethylformamide (DMF) via sonication for 3 h. Secondly, 30 mL of solution containing 18 mmol  $\text{AgNO}_3$  was added to the above PANI aqueous suspension and then the mixture was stirred violently in dark for 12 h. While stirring, the  $\text{Na}_2\text{HPO}_4 \cdot 12\text{H}_2\text{O}$  aqueous solution (30 mL, 6 mmol) was added dropwise to the mixture, followed by 6 h of stirring in dark. Finally, the obtained precipitate was washed with ethanol and de-ionized water several times, and dried in vacuum (60°C) overnight.

### 2.3. Preparation of $\text{Ag}_3\text{PO}_4@\text{MWCNTs@PANI}$

$\text{Ag}_3\text{PO}_4@\text{MWCNTs@PANI}$  was prepared by an in situ deposition-precipitation procedure. Firstly, a certain amount of MWCNTs and PANI was dispersed into 30 mL of DMF via sonication for 3 h. Secondly, 30 mL of 18 mmol  $\text{AgNO}_3$  aqueous solution was added to the above mixed aqueous suspension and then stirred violently in dark for 12 h. And then  $\text{Na}_2\text{HPO}_4 \cdot 12\text{H}_2\text{O}$  aqueous solution (30 mL, 6 mmol) was added dropwise to the mixture with constantly stirring for 6 h in dark. Finally, the obtained olive precipitate was centrifuged and washed with ethanol and de-ionized water several times, and samples were obtained by 12 h of drying at 60 °C. The procedure for the synthesis was illustrated in Fig. S1.

#### 2.4. Characterization

Field emission scanning electron microscopy (FESEM, Hitachi SU8220) and high resolution transmission electron microscope (HRTEM) (TecnaiG2 F20, FEI) were employed to investigate the morphologies and microstructures of samples. The crystal structures of the prepared samples were characterized by X-ray diffractometer (Bruker AXS D8 Advances) with the Cu-K $\alpha$  radiation ( $\lambda = 0.15406$  nm). Chemical compositions of samples were analyzed using X-ray photoelectron spectroscopy (XPS, ESCALAB 250Xi, Thermo Fisher). The UV-vis diffused reflectance spectra (UV-vis DRS) were obtained by UV-vis-NIR spectrophotometer (U-4100, Hitachi). The photoluminescence (PL) spectra were studied through F-7000 fluorescence spectrometer. Raman spectra were obtained on a confocal micro-Raman spectrometer (Horiba Jobin Yvon LabRAM HR800) with an excitation of 633 nm laser light. The BET specific surface of the samples was determined by surface area porosity analyzer (Micromeritics, TriStar II 3020, USA). Zeta potential measurement was carried out using a Zetasizer (Malvern Zetasizer Nano ZS90, UK). The photocurrent response curve and Mott-Schottky plots of the prepared samples were measured by a three-electrode cell in 0.5 mol/L Na<sub>2</sub>SO<sub>4</sub> aqueous solution and a CHI 660D workstation. The as-prepared photocatalysts thin film on fluorine-doped tin oxide (FTO) was used as the working electrode. The other two electrodes were a saturated calomel reference electrode saturated calomel electrode (SCE) and a platinum (Pt) electrode, respectively. The electron spin resonance (ESR) signals of radicals spin-trapped by spin-trapped reagent 5, 5-dimethyl-l-pyrroline N-oxide (DMPO) were examined on a JES FA200 electron paramagnetic resonance spectrometer under visible light irradiation ( $\lambda > 420$  nm). The mineralization ability was tested by total organic carbon (TOC) measurements (Shimadzu TOC-VCPh analyzer). Three-dimensional excitation-emission matrix fluorescence spectra (3D EEMs) were examined by a F-4500 spectrofluorimeter, and the excitation ( $\lambda_{\text{ex}}$ ) and emission wavelengths ( $\lambda_{\text{em}}$ ) were 200–400 and 210–400 nm, respectively.

#### 2.5. Photocatalytic experiments

The photocatalytic activity of the obtained samples was evaluated by phenol and P-nitrophenol decomposition under visible light irradiation. A 300 W Xe lamp with a 420 nm cutoff filter was employed as the light source. The reaction system was cooled by circulating water to maintain at room temperature. In a typical procedure, 50 mg photocatalyst was dispersed in the reaction solution (100 mL, 25 mg/L phenol or 20 mg/L P-nitrophenol). The mixed solution was stirred in dark for 30 min to reach the adsorption-desorption equilibrium. Afterwards, the suspension was exposed to the 300 W Xe lamp. 3 mL of suspension was taken out at a given interval time, and then filtrated through a 0.22  $\mu$ m Millipore filter to remove the particles. The residual concentration was analyzed by high performance liquid chromatography (HPLC, Agilent) equipped with a UV detection and an Agilent ZORBAX SB-C18 (5  $\mu$ m  $\times$  4.6 mm  $\times$  250 mm) reversed-phase column. And the detector was set at the wavelength of 270 nm and 317 nm for phenol and P-nitrophenol, respectively. The operating conditions were as follows: mobile phase of methanol and water (volume ratio: 60/40); flow rate at 1 mL·min<sup>-1</sup>; injection volume by 20  $\mu$ L and column temperature of 30 °C.

### 3. Results and discussion

#### 3.1. Characterization of the as-prepared catalysts

The morphologies and microstructures of the as-prepared samples were investigated by SEM technology. As seen from Fig. 1a, the pure Ag<sub>3</sub>PO<sub>4</sub> presented the polyhedra crystals of varying sizes, with a diameter of about 10–20  $\mu$ m. And some irregular small sphere-like

polyhedral particles with diameters of about 0.42–1.4  $\mu$ m were attached to the large particles (Fig. 1b). Interestingly, as presented in the same scope of SEM image (Fig. 1c–f, 10  $\mu$ m), large Ag<sub>3</sub>PO<sub>4</sub> particles with a diameter of 10–20  $\mu$ m no longer appeared, after the introduction of MWCNTs and PANI, respectively. As shown in Fig. 1g and h, the MWCNTs penetrated into the Ag<sub>3</sub>PO<sub>4</sub> crystals, and the Ag<sub>3</sub>PO<sub>4</sub> particles with a diameter of about 0.38–1.0  $\mu$ m grew along the surface of MWCNTs. This resulted from the electrostatically driven assembly of positively charged Ag<sup>+</sup> on the surface of negatively charged MWCNTs, which further changed the growth pattern, size and morphology of Ag<sub>3</sub>PO<sub>4</sub> crystal particles [7]. Similar phenomena have been reported in our previous studies [8], however, longer MWCNTs with a length of 10–30  $\mu$ m were added in this study, and better bonding between Ag<sub>3</sub>PO<sub>4</sub> crystals and MWCNTs was observed. This was because longer MWCNTs could provide more adsorption sites for Ag<sup>+</sup>. In particular, after the addition of PANI, the large Ag<sub>3</sub>PO<sub>4</sub> crystals were changed into smaller particles with a diameter of 0.15–0.38  $\mu$ m, which were well attached to the surface of PANI (Fig. 1i and j), and the phenomenon was reported for the first time. This was due to the rough surface of PANI and its unique electrostatic properties [20–22], so that Ag<sup>+</sup> was adsorbed uniformly on its surface, thus affecting the growth pattern and size of Ag<sub>3</sub>PO<sub>4</sub> crystal. As shown in the SEM images of Ag<sub>3</sub>PO<sub>4</sub>@MWCNTs@PANI ternary composite (Fig. 1k and l), the size of Ag<sub>3</sub>PO<sub>4</sub> crystal particles was 0.22–0.45  $\mu$ m. Besides, both MWCNTs and PANI were clearly observed, indicating good affinity between these materials. The SEM images of the MWCNTs and PANI were also provided in Fig. S2. Obviously, the SEM observations indicated that both the PANI and MWCNTs have significant influence on the size control of Ag<sub>3</sub>PO<sub>4</sub> crystal particles, and the presence of PANI and MWCNTs were favorable for the formation of smaller Ag<sub>3</sub>PO<sub>4</sub> crystals, which were much helpful to improve the photocatalytic performance of catalysts.

Due to the obviously reduced sizes of Ag<sub>3</sub>PO<sub>4</sub> in the systems of Ag<sub>3</sub>PO<sub>4</sub>@MWCNTs, Ag<sub>3</sub>PO<sub>4</sub>@PANI and Ag<sub>3</sub>PO<sub>4</sub>@MWCNTs@PANI compared to pure Ag<sub>3</sub>PO<sub>4</sub>, the BET specific surface of the samples were determined, and the data has been provided in Table S1. The BET specific surface area of the Ag<sub>3</sub>PO<sub>4</sub>, Ag<sub>3</sub>PO<sub>4</sub>@MWCNTs, Ag<sub>3</sub>PO<sub>4</sub>@PANI and Ag<sub>3</sub>PO<sub>4</sub>@MWCNTs@PANI are 0.18, 1.64, 1.55 and 1.61 m<sup>2</sup>/g, respectively. After the addition of MWCNTs, the specific surface area of Ag<sub>3</sub>PO<sub>4</sub>@MWCNTs and Ag<sub>3</sub>PO<sub>4</sub>@PANI was increased, which resulted from the MWCNTs possessing big surface area, besides, the size of Ag<sub>3</sub>PO<sub>4</sub> has been decreased apparently [24]. Consequently, more active species and reactants can be absorbed on the surface of photocatalyst because of the larger surface area, which are beneficial to improving its photocatalytic activity [25,26].

Additional cross section elemental mappings combined with EDS analysis for Ag<sub>3</sub>PO<sub>4</sub>@MWCNTs@PANI composite were also performed. As shown in Fig. 2, Ag, P, O, C and N elements were all clearly presented. The results indicated that Ag<sub>3</sub>PO<sub>4</sub> particles were well-distributed on the surface of PANI. In order to obtain the detailed structural information, the high-resolution transmission electron microscopy (HRTEM) image of the photocatalysts was recorded and provided in Fig. 3. As shown, the hollow MWCNTs with an outer diameter of about 20 nm passed through the silver phosphate crystals, and good interfacial contact between PANI and Ag<sub>3</sub>PO<sub>4</sub> could also be observed. The interplanar spacing of 0.299 nm was clearly observed, which corresponds to (200) crystallographic planes of Ag<sub>3</sub>PO<sub>4</sub> and is consistent with JCPDS card No.06-0505. The results indicated that the MWCNTs and PANI were successfully introduced into Ag<sub>3</sub>PO<sub>4</sub>@MWCNTs@PANI composite, and the good binding among Ag<sub>3</sub>PO<sub>4</sub>, MWCNTs and PANI was built.

In order to investigate the crystal structure properties of the prepared samples, X-ray diffraction (XRD) patterns were provided in Fig. 4, from which the crystal structure of the Ag<sub>3</sub>PO<sub>4</sub>, Ag<sub>3</sub>PO<sub>4</sub>@MWCNTs, Ag<sub>3</sub>PO<sub>4</sub>@PANI and Ag<sub>3</sub>PO<sub>4</sub>@MWCNTs@PANI could be indexed to the body-centered cubic structure of Ag<sub>3</sub>PO<sub>4</sub> (JCPDS No. 06-0505). Moreover, no characteristic diffraction peaks of PANI were observed in

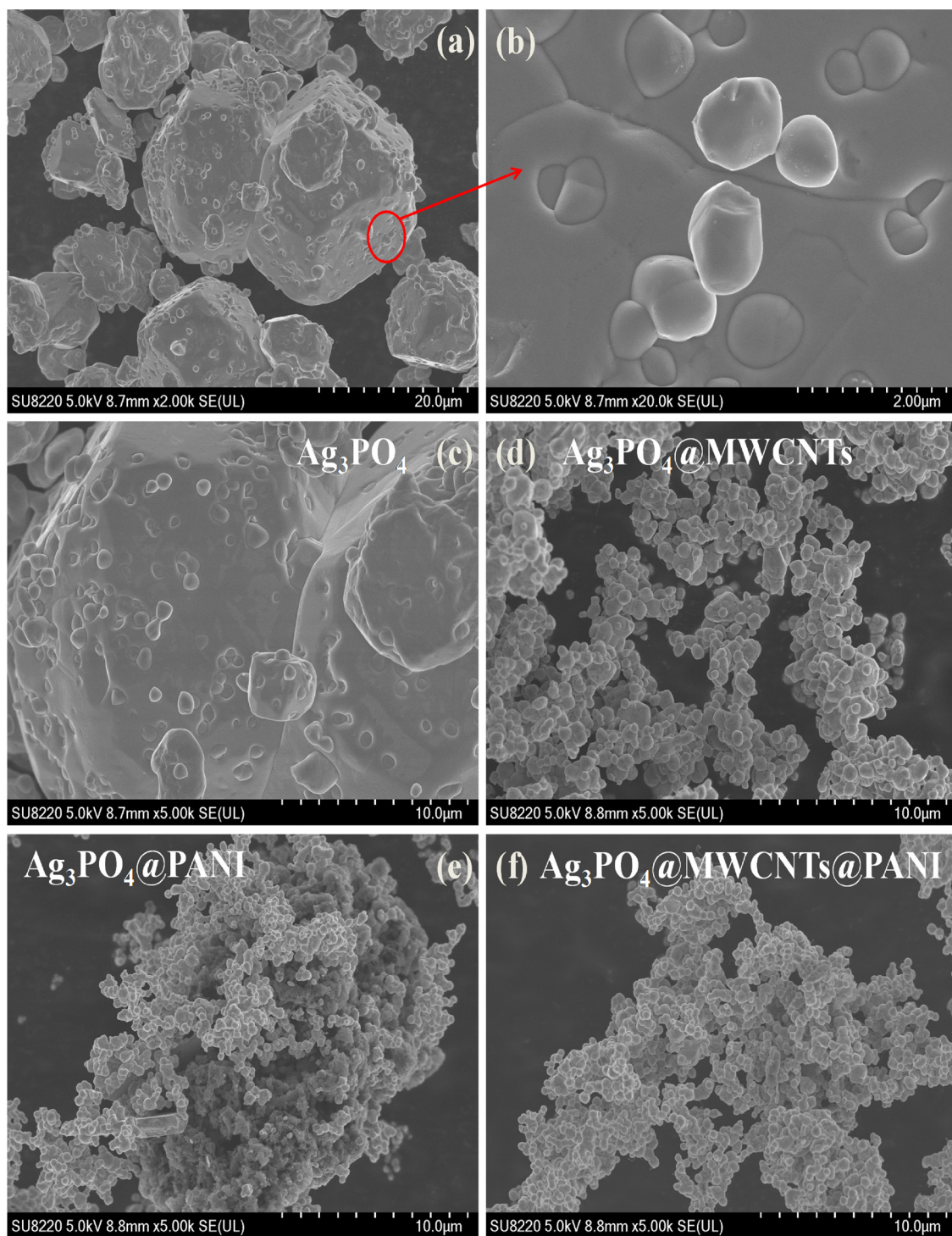


**Fig. 1.** SEM images of Ag<sub>3</sub>PO<sub>4</sub> (a,b,c), Ag<sub>3</sub>PO<sub>4</sub>@MWCNTs composite (d,g,h), Ag<sub>3</sub>PO<sub>4</sub>@PANI composite (e,i,j) and Ag<sub>3</sub>PO<sub>4</sub>@MWCNTs@PANI composite (f,k,l).

Ag<sub>3</sub>PO<sub>4</sub>@PANI and Ag<sub>3</sub>PO<sub>4</sub>@MWCNTs@PANI composite because the PANI in the composites exists in amorphous form [4]. The diffraction peaks at  $2\theta = 20.9^\circ, 29.7^\circ, 33.3^\circ, 36.6^\circ, 42.5^\circ, 47.8^\circ, 52.7^\circ, 55.0^\circ, 57.3^\circ, 61.6^\circ$  and  $71.9^\circ$  could be indexed to the (110), (200), (210), (211), (220), (310), (222), (320), (321), (400) and (421) planes for Ag<sub>3</sub>PO<sub>4</sub>, respectively. Although the positions of diffraction peaks were almost the same, evident changes in the intensity ratios of various peaks of Ag<sub>3</sub>PO<sub>4</sub> were observed in different samples. According to the findings in previous studies, the significant change of peak intensity ratio of different crystal planes revealed the changes of the crystal facet exposure [3]. The intensity ratio of the (110), (200) and (210) peaks were

1:1.094:6.373, 1:1.162:7.344, 1:2.202:7.571 and 1:1.181:9.055 for the Ag<sub>3</sub>PO<sub>4</sub>, Ag<sub>3</sub>PO<sub>4</sub>@MWCNTs, Ag<sub>3</sub>PO<sub>4</sub>@PANI and Ag<sub>3</sub>PO<sub>4</sub>@MWCNTs@PANI, respectively. This change indicated that the crystal facet exposure of Ag<sub>3</sub>PO<sub>4</sub> was affected by the addition of MWCNTs and PANI, implying the changes of microstructure and morphology of crystals. The results of XRD were well consistent with the findings of the SEM, which further confirmed the influence of MWCNTs and PANI on the microstructure of Ag<sub>3</sub>PO<sub>4</sub> crystal.

The elemental chemical compositions and chemical status of Ag<sub>3</sub>PO<sub>4</sub>@MWCNTs@PANI composite were determined by the X-ray photoelectron spectroscopy (XPS). As presented in Fig. 5a, all elements

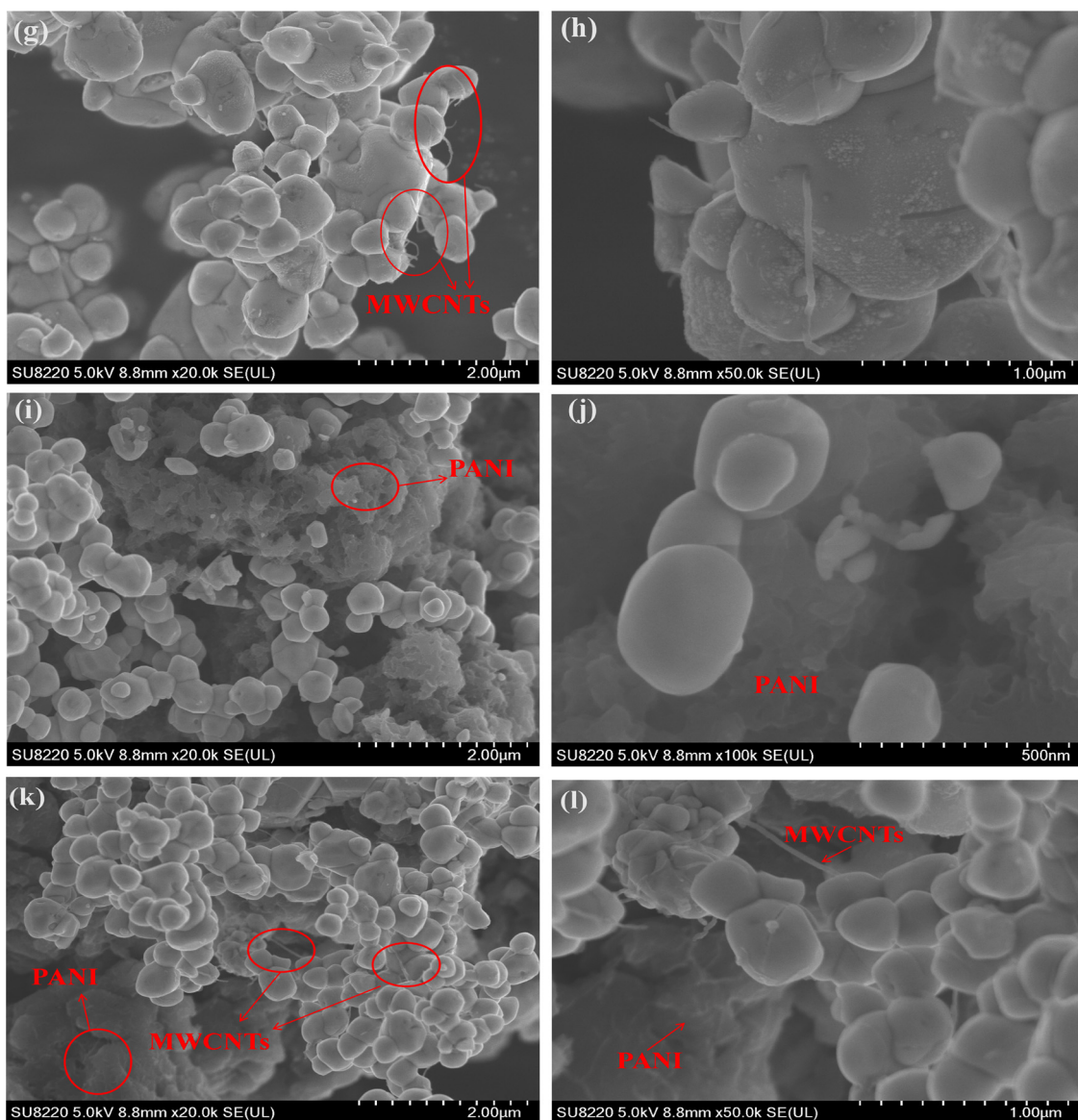


Fig. 1. (continued)

of Ag, P, O, C and N could be found in the XPS survey spectrum. The Ag 3d<sub>3/2</sub> and Ag 3d<sub>5/2</sub> peaks could be observed at 373.4 and 367.4 eV of binding energy, respectively, indicating the existence of Ag<sup>+</sup> in the composite (Fig. 5b). The P 2p spectrum was provided in Fig. 5c, the typical peak located at 132.6 eV corresponded to the phosphorus coming from PO<sub>4</sub><sup>3-</sup>. As shown in Fig. 5d, the O 1s spectrum of the composite could be deconvoluted into two peaks, the peak centered at 530.1 eV was associated with the lattice O in Ag<sub>3</sub>PO<sub>4</sub>, and the other positioned at 531.5 eV was assigned to the -C=O (carbonyl) functional group in MWCNTs [27,28]. As shown in Fig. 5e, the C 1s peaks could be divided into two different peaks at 284.3 eV and 286.2 eV, respectively. The peak at 284.3 eV was arising from the PANI backbones, adventitious carbon and sp<sup>2</sup>-hybridized carbon of MWCNTs, while the peak at 286.2 eV can be assigned to hydroxyl carbon [29,30]. The N 1s XPS spectrum was displayed in Fig. 5f, three typical peaks were located at 396.2 eV, 400 eV and 404.9 eV, which could be attributed to the -N= (quinoid imine), -NH- (benzoid amine) and positively charged nitrogen (-HN<sup>+</sup>- and -HN<sup>+</sup>=), respectively [29]. The XPS results further confirmed the successful combination of Ag<sub>3</sub>PO<sub>4</sub>, MWCNTs and PANI in Ag<sub>3</sub>PO<sub>4</sub>@MWCNTs@PANI composite.

UV-vis diffuse reflectance spectrum (DRS) was measured to evaluate the optical absorption properties of as-prepared photocatalysts. As

illustrated in Fig. 6a, Ag<sub>3</sub>PO<sub>4</sub>, Ag<sub>3</sub>PO<sub>4</sub>@MWCNTs, Ag<sub>3</sub>PO<sub>4</sub>@PANI and Ag<sub>3</sub>PO<sub>4</sub>@MWCNTs@PANI all exhibited excellent absorption performance at the wavelength of less than 520 nm. However, after the addition of PANI and MWCNTs, the absorbance of composite materials was obviously enhanced, and good light absorption was still available in the range of 520–800 nm. The enhanced absorbing ability indicated that MWCNTs and PANI were successfully incorporated into Ag<sub>3</sub>PO<sub>4</sub> and contributed to promoting the optical absorption capacity. The band gap energy (Eg) of a semiconductor could be calculated by the Kubelka-Munke equation:

$$(\alpha h\nu)^n = A(h\nu - E_g) \quad (1)$$

Where  $\alpha$ ,  $h$ ,  $\nu$ ,  $A$  and  $E_g$  represents absorption coefficient, Planck constant, light frequency, proportionality constant, and band gap energy, respectively. And  $n$  value depends on the type of optical transition of semiconductors ( $n = 2$  for direct transition and  $n = 1/2$  for indirect transition) [31]. As shown the inset image in Fig. 6a, the band gap energy (Eg) of Ag<sub>3</sub>PO<sub>4</sub> was estimated to be 2.26 eV. Moreover, Mott-Schottky plot was used to characterize the flat band potential of different samples [8], and the results were provided in Fig. 6b. The curves with overall positive slopes indicated they were typical n-type semiconductors. The Mott-Schottky equation was shown as follows:

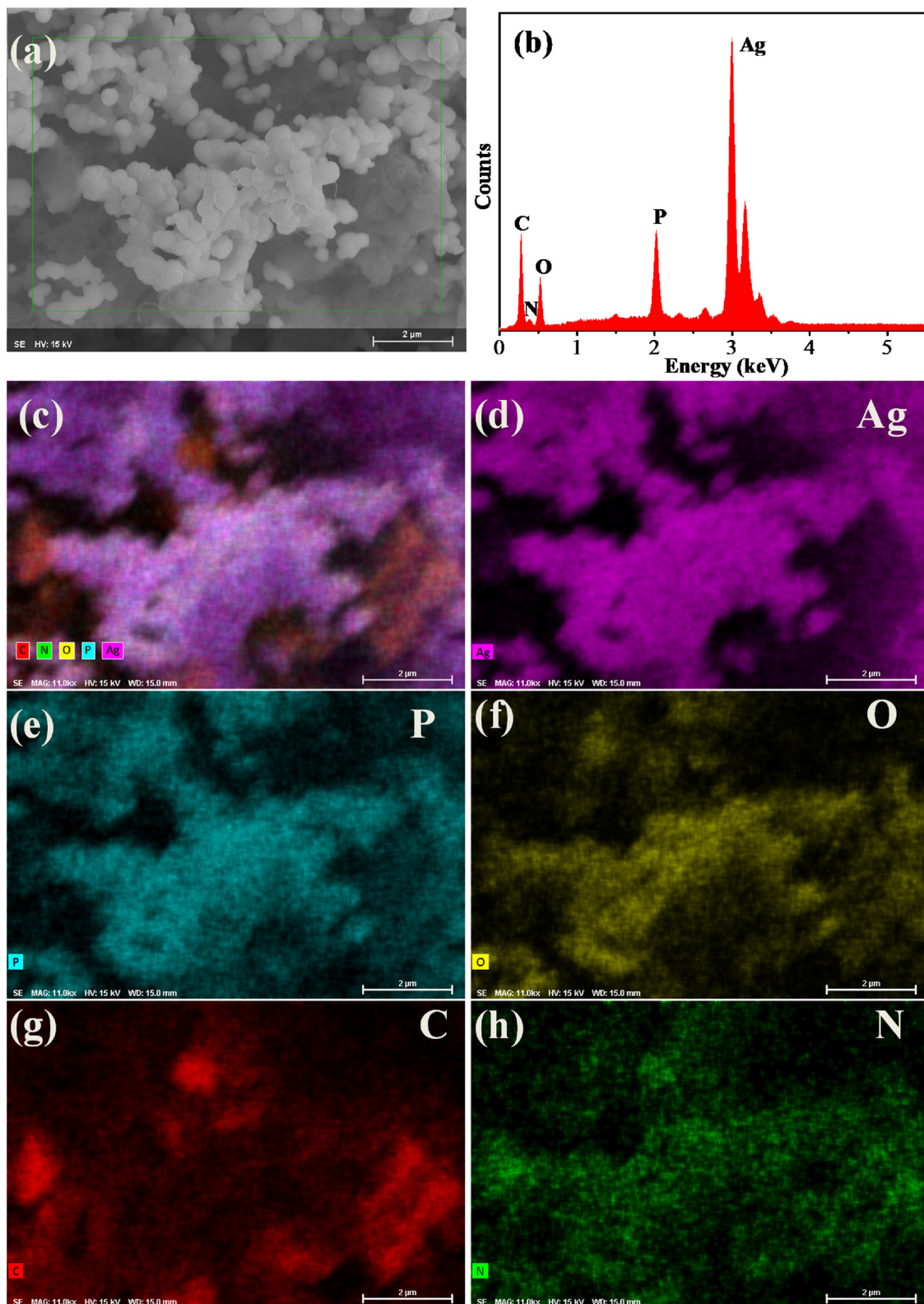


**Fig. 2.** SEM-EDS elemental mapping images of  $\text{Ag}_3\text{PO}_4@\text{MWCNTs@PANI}$  composite.

$$\frac{1}{C_{SC}^2} = \frac{2}{e\epsilon\epsilon_0 N} \left( E - E_{fb} - \frac{KT}{e} \right) \quad (2)$$

Where  $C_{SC}$  is the capacitance of the space charge region,  $\epsilon$  is the dielectric constant of the semiconductor,  $\epsilon_0$  is the permittivity of free space,  $N$  is the donor density,  $k$  is Boltzmann's constant,  $T$  is the temperature,  $q$  is the electronic charge,  $E$  and  $E_{fb}$  is the applied potential

and flat band potential, respectively. The applied potential ( $E$ ) and flat band potential ( $E_{fb}$ ) could be calculated by x-intercepts of the linear region, which were all found to be 0.42 V versus the saturated calomel electrode (SCE) for the four kinds of photocatalysts. As the value of  $KT/e$  was 0.0257, so the flat potential was calculated to be 0.39 V vs. SCE. The potential of the conduction band in the n-type semiconductor is

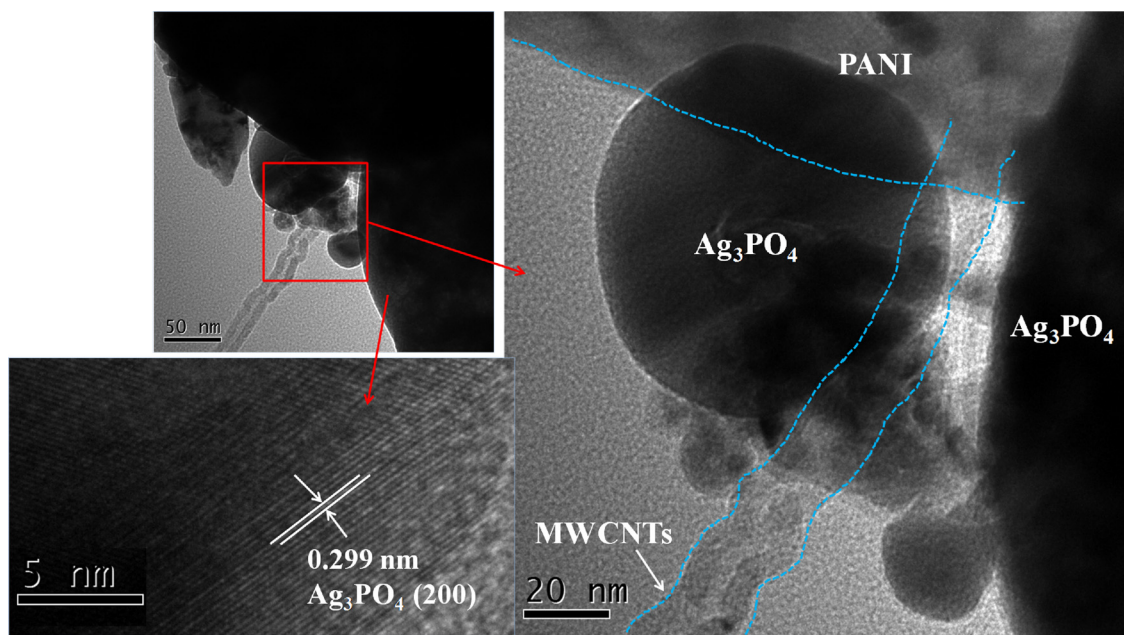


Fig. 3. HRTEM images analysis of  $\text{Ag}_3\text{PO}_4$ @MWCNTs@PANI composite.

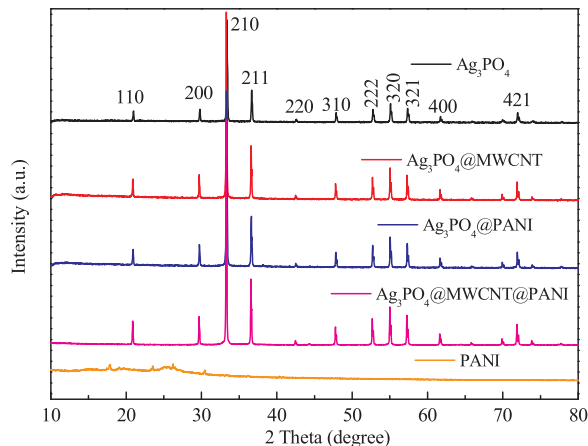


Fig. 4. XRD pattern of as-prepared samples.

more negative by 0.2 V than that of the flat band potential [32]. The conduction band potential ( $E_{\text{CB}}$ ) of  $\text{Ag}_3\text{PO}_4$  was determined to be 0.19 V vs. SCE (equivalent to 0.43 V vs. NHE). Because the band gap energy ( $E_g$ ) of  $\text{Ag}_3\text{PO}_4$  was 2.26 eV, the valence band potential ( $E_{\text{VB}}$ ) of  $\text{Ag}_3\text{PO}_4$  could be calculated as 2.69 V vs. NHE. Moreover, the above results also suggested that the addition of MWCNTs and PANI did not change the flat band potential of  $\text{Ag}_3\text{PO}_4$ .

Raman spectra were performed to obtain the information on the interface interaction of  $\text{Ag}_3\text{PO}_4$ , MWCNTs and PANI. As shown in Fig. 7a, the distinct peak at  $912 \text{ cm}^{-1}$  could be ascribed to the motion of terminal oxygen bond vibration of phosphate group, and the peak located at  $556 \text{ cm}^{-1}$  belonged to the symmetric stretch of P—O—P bonds [33,34]. For the Raman spectrum of PANI, the peaks at  $1173 \text{ cm}^{-1}$ ,  $1347 \text{ cm}^{-1}$ ,  $1476 \text{ cm}^{-1}$  and  $1596 \text{ cm}^{-1}$  could be assigned to the C—H bend mode,  $\text{C}=\text{N}^+$  in the benzene ring (polaron structure), quinonoid unit vibration mode, and the vibrational mode of benzenoid unit, respectively [21,29,35]. After the incorporation of PANI, the Raman bands appeared at  $1173 \text{ cm}^{-1}$  in the  $\text{Ag}_3\text{PO}_4$ @PANI and  $\text{Ag}_3\text{PO}_4$ @MWCNTs@PANI composite were moved to higher wavenumber, while two characteristic peaks at  $1347 \text{ cm}^{-1}$  and  $1596 \text{ cm}^{-1}$  were both shifted to lower wavenumber (Fig. 7b). Similar phenomena were also reported in previous studies, the red shift of these bands was due to

weakening bond strengths of  $\text{C}=\text{N}$  ( $\text{C}=\text{C}$ ) and  $\text{C}—\text{N}$  [18,21,34]. For the Raman spectra of the MWCNTs and  $\text{Ag}_3\text{PO}_4$ @MWCNTs, two typical Raman shifts centered at  $1341 \text{ cm}^{-1}$  and  $1592 \text{ cm}^{-1}$  corresponded to D and G bands, respectively. The D bands were related to the amorphous/disordered carbon ( $\text{sp}^3$ ) and G bands to the graphitic carbon ( $\text{sp}^2$ ). After adding MWCNTs, the  $I_D/I_G$  ratio decreased from 1.64 to 1.07, which indicated that there were  $\text{sp}^3$ -hybridized carbons changed to  $\text{sp}^2$ -hybridized carbons [35–38]. The above results implied that the hybridization between  $\text{Ag}_3\text{PO}_4$  and PANI result in an intense interface interaction between PANI and  $\text{Ag}_3\text{PO}_4$ , and strong interactions have occurred between  $\text{Ag}_3\text{PO}_4$  and MWCNTs. These hybrid effects play an important role in promoting the separation of photogenerated carriers and enhancing the photocatalytic performance of composite photocatalyst. The results of SEM, EDS, HRTEM, XRD, XPS, DRS and Raman spectra all indicated that  $\text{Ag}_3\text{PO}_4$ , MWCNTs and PANI were closely combined in  $\text{Ag}_3\text{PO}_4$ @MWCNTs@PANI composite, and fully demonstrated that there was a dense interfacial interaction between them.

In order to evaluate the separation efficiency of photogenerated electron-hole pairs, the photoluminescence (PL) spectroscopy study and test of transient photocurrent responses under visible light irradiation were carried out. As shown in Fig. 8a,  $\text{Ag}_3\text{PO}_4$  displayed the highest PL intensity, indicating the easy recombination of photogenerated electron-hole pairs. Compared with pure  $\text{Ag}_3\text{PO}_4$ , the binary and ternary samples all presented much lower PL peak intensity, and the  $\text{Ag}_3\text{PO}_4$ @MWCNTs@PANI composite exhibited the weakest luminous peak intensity, demonstrating its excellent carrier separation ability. These results indicated the separation efficiency of photogenerated electrons and holes was significantly improved with the addition of MWCNTs and PANI. Moreover, the transient photocurrent responses of  $\text{Ag}_3\text{PO}_4$ ,  $\text{Ag}_3\text{PO}_4$ @MWCNTs,  $\text{Ag}_3\text{PO}_4$ @PANI and  $\text{Ag}_3\text{PO}_4$ @MWCNTs@PANI were illustrated in Fig. 8b. Obvious changes of photocurrent response could be observed when turning on and off the visible light irradiation. It could be clearly seen that the binary and ternary photocatalysts showed a significantly enhanced photocurrent density than pure  $\text{Ag}_3\text{PO}_4$ , and the  $\text{Ag}_3\text{PO}_4$ @MWCNTs@PANI composite exhibited the strongest photocurrent response among all catalysts. The enhanced photocurrents also indicated much higher separation efficiency of photogenerated electron-hole pairs with the addition of MWCNTs and PANI. These resulted from that the MWCNTs can act as the capture trap of the photogenerated electrons and PANI as the photogenerated hole-

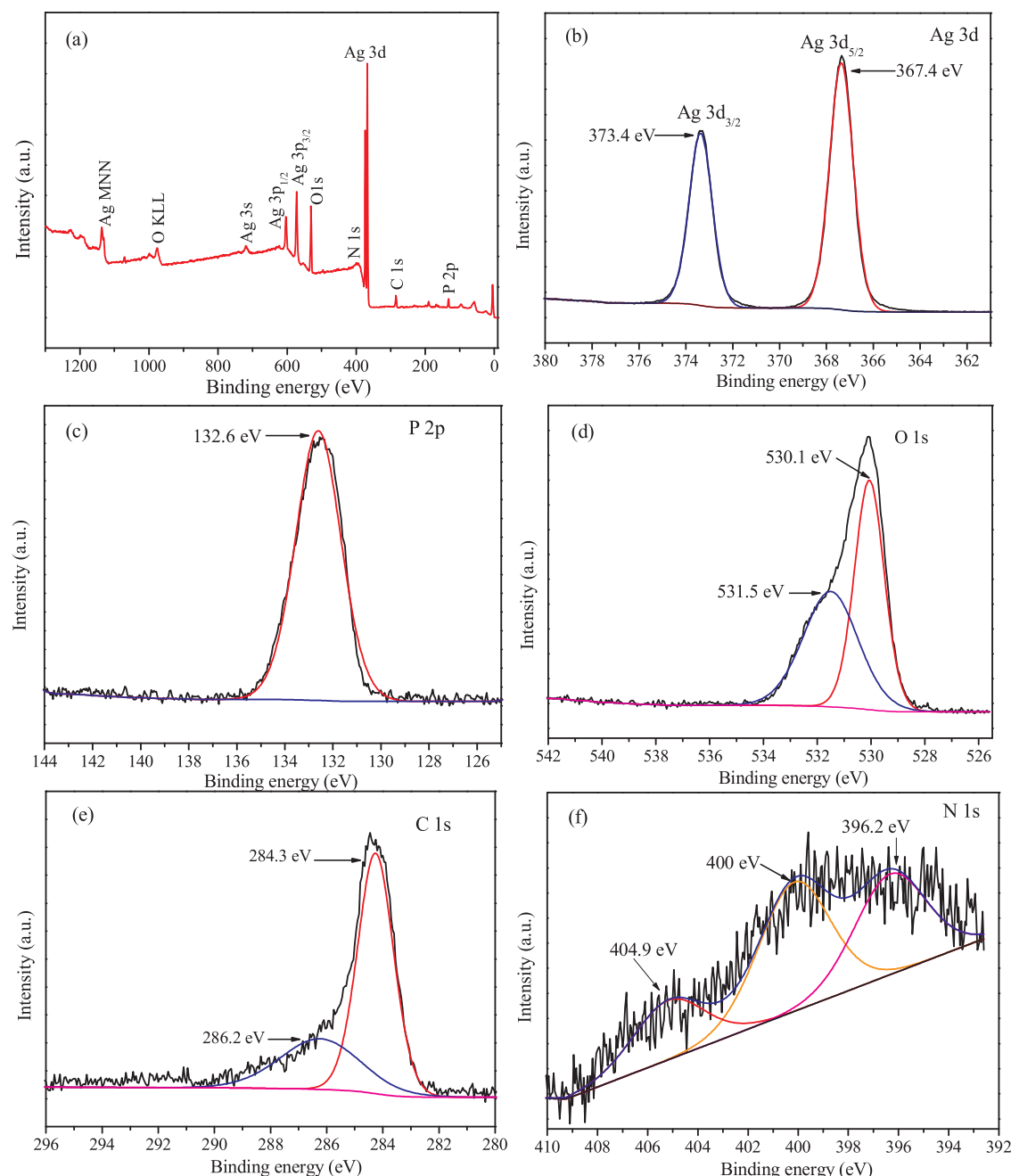


Fig. 5. (a) XPS survey spectra; high resolution XPS spectrum of (b) Ag 3d, (c) P 2p, (d) O 1s, (e) C 1s and (f) N 1s.

transporting material, the synergistic effect between them promoted the rapid transfer and separation of photogenerated carries.

### 3.2. Photocatalytic performance and mineralization ability

Phenol and p-nitrophenol, as a kind of widespread organic pollutant, were selected to evaluate the photocatalytic activity of as-prepared photocatalyst. The 50 mg photocatalyst was added to 20 mg/L of phenol solution (100 mL). After 30 min of dark reaction, 300 W Xe lamp ( $\lambda > 420$  nm) was employed as the artificial light source to carry out the photodegradation experiment. As shown in Fig. 9a, single  $\text{Ag}_3\text{PO}_4$  displayed poor photocatalytic activity with only 33.26% of phenol degradation after 20 min irradiation. Compared with  $\text{Ag}_3\text{PO}_4$ , all  $\text{Ag}_3\text{PO}_4@\text{MWCNTs}$  composite exhibited much higher degradation performance. Especially, in all binary complexes, 0.1%MWCNTs@ $\text{Ag}_3\text{PO}_4$  showed the highest photocatalytic activity, which could degrade

92.64% of phenol after only 8 min of exposure to visible light, and the phenol was completely degraded in the next few minutes. Moreover, the corresponding reaction kinetic curves for the samples were provided in Fig. 9d. Obviously, the photodegradation process followed pseudo-first-order kinetics and the maximum rate constant  $k$  (for 0.1% MWCNTs@ $\text{Ag}_3\text{PO}_4$ ,  $0.35 \text{ min}^{-1}$ ), was about 19.4 times than that of pure  $\text{Ag}_3\text{PO}_4$  ( $0.018 \text{ min}^{-1}$ ). The results indicated that the photocatalytic activity of  $\text{Ag}_3\text{PO}_4$  was significantly enhanced with the addition of MWCNTs, which could be attributed to the formation of smaller  $\text{Ag}_3\text{PO}_4$  crystal particles with the doping of MWCNTs, and its excellent conductivity made it an effective acceptor of the photogenerated electrons, hence the significantly improved separation efficiency of photogenerated carrier. In order to observe photocatalytic performance improvement of the prepared photocatalyst more clearly, the concentration of phenol was increased to 25 mg/L under the same conditions. As shown in Fig. 9b, phenol was almost not degraded in the

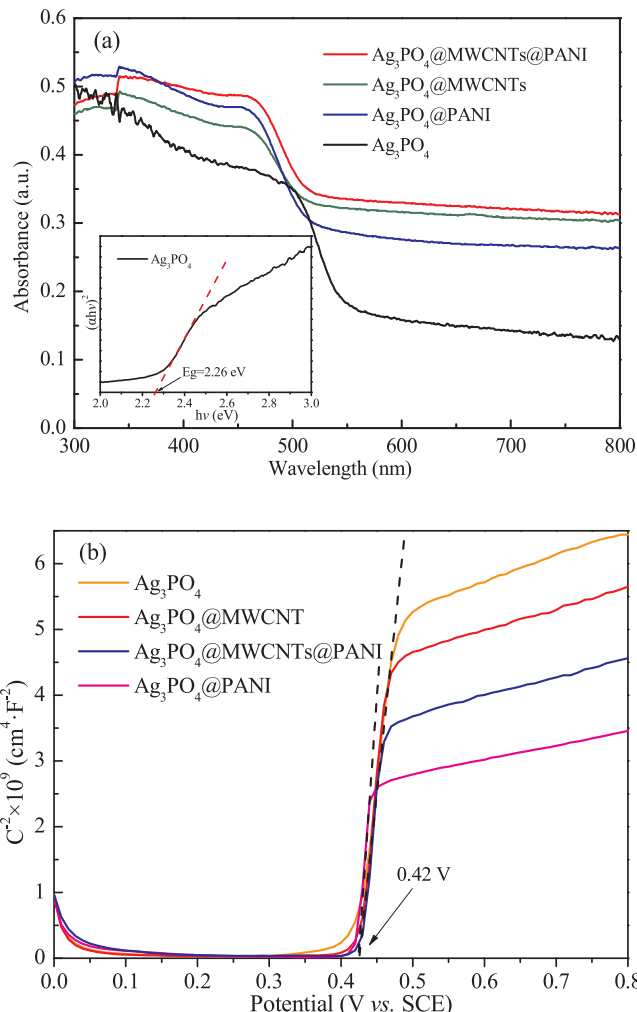


**Fig. 6.** (a) UV-vis diffuse reflectance spectra of different samples, and the inset image is the band gap energy of  $\text{Ag}_3\text{PO}_4$ ; (b) Mott-Schottky plots of different samples.

presence of PANI, and only 27.7% of phenol was degraded in 20 min over pure  $\text{Ag}_3\text{PO}_4$ . Comparing with  $\text{Ag}_3\text{PO}_4$ , PANI,  $\text{Ag}_3\text{PO}_4@\text{PANI}$  and  $\text{Ag}_3\text{PO}_4@\text{MWCNTs}$  composite, all ternary  $\text{Ag}_3\text{PO}_4@\text{MWCNTs@PANI}$  composite showed much superior photocatalytic performance, and the  $\text{Ag}_3\text{PO}_4@\text{MWCNTs@3\%PANI}$  composite exhibited the highest degradation efficiency (100%) within 20 min of visible-light irradiation. The values of the rate constant ( $k$ ) were shown in Fig. 9e, the rate constant ( $k$ ) for the phenol degradation was greatest for  $\text{Ag}_3\text{PO}_4@\text{MWCNTs@3\%PANI}$  ( $0.35 \text{ min}^{-1}$ ), which was about 21.9 times than that of pure  $\text{Ag}_3\text{PO}_4$  ( $0.016 \text{ min}^{-1}$ ). And it was up to 2.19 and 2.69-fold higher than that of  $\text{Ag}_3\text{PO}_4@\text{PANI}$  ( $0.16 \text{ min}^{-1}$ ) and  $\text{Ag}_3\text{PO}_4@\text{MWCNTs}$  ( $0.13 \text{ min}^{-1}$ ), respectively. Furthermore, p-nitrophenol was chosen as another model pollutant to evaluate the photocatalytic activities of the prepared photocatalysts. As shown in Fig. 9c, the  $\text{Ag}_3\text{PO}_4@\text{MWCNTs@3\%PANI}$  composite still exhibited the highest activity. The rate constant ( $k$ ) for the p-nitrophenol degradation was greatest for  $\text{Ag}_3\text{PO}_4@\text{MWCNTs@PANI}$  ( $0.43 \text{ min}^{-1}$ ), followed by  $\text{Ag}_3\text{PO}_4@\text{PANI}$  ( $0.28 \text{ min}^{-1}$ ),  $\text{Ag}_3\text{PO}_4@\text{MWCNTs}$  ( $0.25 \text{ min}^{-1}$ ), and then the lowest for  $\text{Ag}_3\text{PO}_4$  ( $0.043 \text{ min}^{-1}$ ) (Fig. 9f). Notably, the photodegradation rate of  $\text{Ag}_3\text{PO}_4@\text{MWCNTs@PANI}$  composite was about 10 times higher than that of pure  $\text{Ag}_3\text{PO}_4$ . Besides, the HPLC chromatogram during the photodegradation of phenol and p-nitrophenol over  $\text{Ag}_3\text{PO}_4@\text{MWCNTs@PANI}$  was provided in Fig. S3a and Fig. S3b, respectively. The phenol and p-nitrophenol showed the characteristic peak with retention time of 3.9 min and 4.54 min, respectively. The

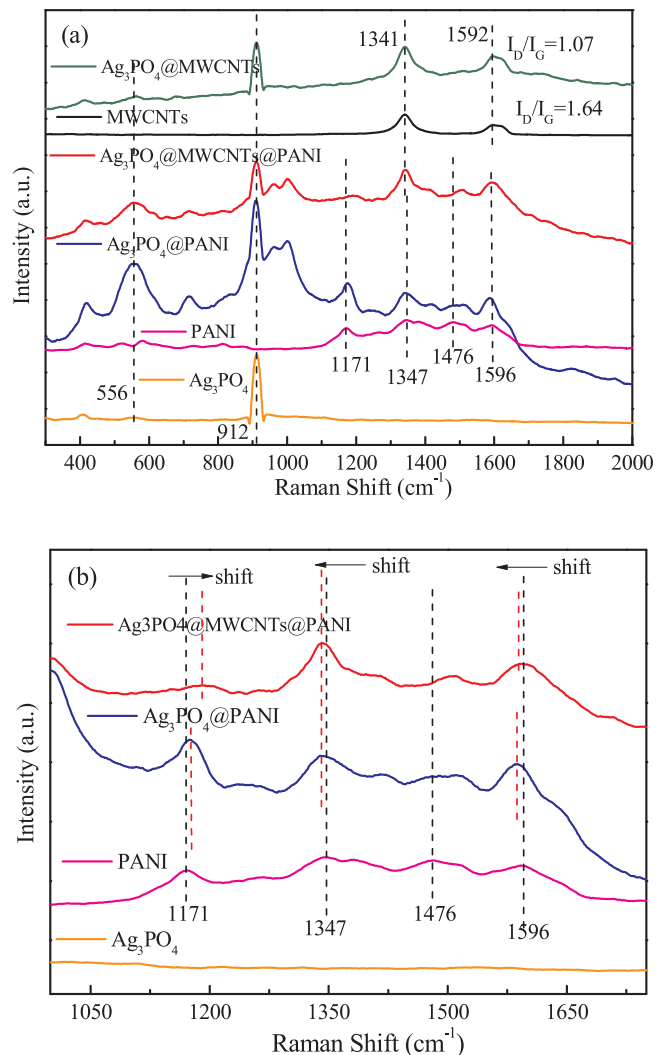


**Fig. 7.** Raman spectra of different samples.

typical peaks became weaker with increasing irradiation time and disappeared completely during the photodegradation, indicating phenol and p-nitrophenol were completely removed owing to the excellent photocatalytic activity of  $\text{Ag}_3\text{PO}_4@\text{MWCNTs@PANI}$ . The above results indicated that the combination of  $\text{Ag}_3\text{PO}_4$  with MWCNTs and PANI was an effective way to improve the photocatalytic activity. The addition of MWCNTs and PANI not only significantly reduced the crystal size of silver phosphate, but also improved the charge carrier separation by the formation of strong interfacial interaction among different components.

Three-dimensional excitation-emission matrix fluorescence spectra (3D EEMs) technology and total organic carbon (TOC) measurements were also employed to deeply investigate the phenol degradation. The phenol aqueous solution treated by  $\text{Ag}_3\text{PO}_4@\text{MWCNTs@PANI}$  composite, was sampled after 30 min adsorption in dark and after the visible light irradiation time of 1, 3, 5, 8 and 20 min, respectively. As shown in Fig. 10A, one fluorescence peak at  $E_x/E_m = 260\text{--}280 \text{ nm}/280\text{--}320 \text{ nm}$  was detected in the solution after dark reaction (Fig. 10a). Under visible light (Fig. 10b–f), the peak intensity gradually decreased, and after 8 min of irradiation, there was only a weak peak which finally disappeared afterwards. In addition, there was no fluorescent signal of other compounds, such as humic acid ( $E_x/E_m = 200\text{--}400 \text{ nm}/350\text{--}400 \text{ nm}$ ), appearing during degradation [39,40]. It indicated that the phenol might be directly decomposed into  $\text{CO}_2$  and  $\text{H}_2\text{O}$  or mineralized into other intermediates. The total organic carbon (TOC)

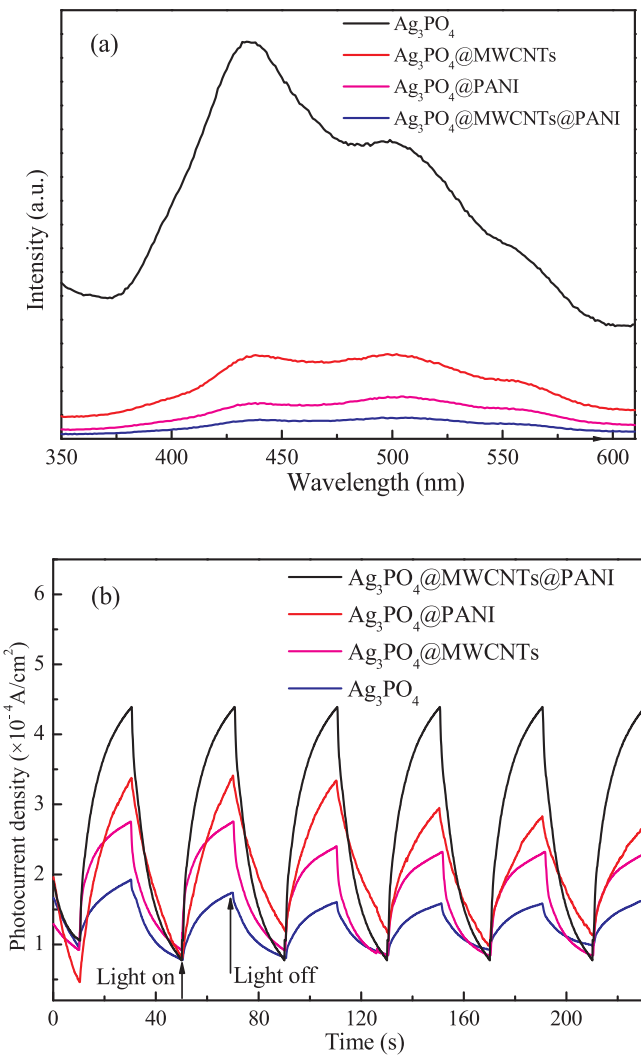


**Fig. 8.** (a) Photoluminescence (PL) spectra of the prepared samples; (b) photocurrent response density of as-prepared samples.

removal rate was therefore determined to assess the mineralization efficiency. As presented in Fig. 10B, the phenol mineralization was only 19.66% for pure  $\text{Ag}_3\text{PO}_4$ , while the mineralization efficiency reached to 72.02%, 75.41%, and 83.59% within the irradiation time of 20 min for the  $\text{Ag}_3\text{PO}_4@\text{MWCNTs}$ ,  $\text{Ag}_3\text{PO}_4@\text{PANI}$  and  $\text{Ag}_3\text{PO}_4@\text{MWCNTs@PANI}$  composite, respectively. The result was in good accordance with that of 3D EEMs, demonstrating that  $\text{Ag}_3\text{PO}_4@\text{MWCNTs@PANI}$  composite exhibited superior mineralization ability toward phenol degradation.

### 3.3. Photostability and recyclability

The photostability investigation of as-prepared photocatalysts was displayed in Fig. 11a. After five cycles, the degradation rate of phenol by the pure  $\text{Ag}_3\text{PO}_4$  decreased from initial 27.7% to 16.4%, and the removal efficiency was reduced by 40.8%. In contrast, it could be clearly seen that the photocatalytic activity of  $\text{Ag}_3\text{PO}_4@\text{MWCNTs@PANI}$  composite didn't reduce after three successive cycles, and the photodegradation efficiency of phenol was still up to 100%. Moreover, the removal rate could still reach 91.49% in the fourth run, and 87.5% phenol could be degraded over  $\text{Ag}_3\text{PO}_4@\text{MWCNTs@PANI}$  composite after five recycling runs. Compared with the first time, the removal efficiency was reduced by 12.5% in the fifth run. The results indicated that the  $\text{Ag}_3\text{PO}_4@\text{MWCNTs@PANI}$  composite had a much higher stability in the photocatalytic reaction under visible light irradiation,

comparing with the pure  $\text{Ag}_3\text{PO}_4$ . Phenol decomposition by  $\text{Ag}_3\text{PO}_4@\text{MWCNTs}$  and  $\text{Ag}_3\text{PO}_4@\text{PANI}$  composite experienced about 21.8% and 24.3% reduction, respectively. After five cycles, the degradation rate of phenol by  $\text{Ag}_3\text{PO}_4@\text{MWCNTs}$  and  $\text{Ag}_3\text{PO}_4@\text{PANI}$  decreased from 95.47% to 74.62%, and 97.66% to 73.96% correspondingly. The above results indicated that the photostability of  $\text{Ag}_3\text{PO}_4$  were greatly improved after the addition of MWCNTs and PANI, which also further confirmed that the  $\text{Ag}_3\text{PO}_4@\text{MWCNTs@PANI}$  composite was effective and stable during the photocatalysis, and the co-modified method obviously enhanced both the photocatalytic performance and photostability of single-component. The significant loss for the photocatalytic performance of  $\text{Ag}_3\text{PO}_4$  was attributed to the partial reduction of  $\text{Ag}_3\text{PO}_4$  into  $\text{Ag}^\circ$  by photogenerated electrons. However, the hybridized MWCNTs and PANI could be used as acceptor of the photogenerated electrons and capture trap of photogenerated hole, respectively, to separate the electron-hole pairs quickly, thus dramatically improving the photoactivity and photostability of catalyst. The above results were in good agreement with the analysis of PL and transient photocurrent responses. Moreover, the XRD of the fresh and used  $\text{Ag}_3\text{PO}_4@\text{MWCNTs@PANI}$  composite after 5 cycles were provided for comparison. As shown in Fig. 11b, there were no evident crystalline structural changes after the photocatalytic reaction. The weak characteristic peak at 2θ value of 38.12° could be ascribed to the (111) crystal planes of metallic Ag, suggesting only a small amount of metallic Ag generated in the photodegradation procedure. According to previous reports, a large amount of  $\text{Ag}^\circ$  deposited on the catalyst surface not only destroyed its crystal structure but also reduced its light absorption efficiency, which sequentially influenced its photocatalytic activity and stability [41]. However, the existence of minor amount of Ag did not reduce the photocatalytic efficiency, but instead enhance photoactivity. Because a small amount of Ag could act as the charge transmission-bridge to accelerate the charge transfer rate and promote the separation of electron-hole pairs due to its Schottky barriers at the metal-semiconductor interfaces [31,39,42], and the localized surface plasmon resonance (LSPR) of Ag nanoparticles on photocatalyst could also enhance the photocatalytic activity [43–45]. For example, Liu et. al [45] prepared the  $\text{Ag}/\text{Ag}_3\text{PO}_4$  photocatalyst and found that the LSPR produced by the collective oscillations of surface electrons on Ag nanoparticles could induce enhancement of the local inner electromagnetic field. The electrons and holes generated by the  $\text{Ag}_3\text{PO}_4$  could be separated efficiently with the help of the local electromagnetic field and the excellent conductivity of Ag nanoparticles, and the electrons could be transferred quickly and induced away from  $\text{Ag}_3\text{PO}_4$  as far as possible, instead of remaining in the  $\text{Ag}_3\text{PO}_4$  lattice. So the  $\text{Ag}/\text{Ag}_3\text{PO}_4$  composite could show efficient activity and remain stable.

### 3.4. Effects of coexisting inorganic salts and the pH value

Considering that there were various coexisting ions and pH values in practical wastewater systems, the effects of different pH values and inorganic salts on the phenol degradation were thus taken into discussion. Several common inorganic ions with the concentration of 0.1 mol/L were added to the reaction system [46–49], and the results were presented in Fig. 12a. No significant difference could be observed in the degradation curves of the solutions containing  $\text{Na}_2\text{SO}_4$  and  $\text{NaNO}_3$ , indicating that  $\text{SO}_4^{2-}$ ,  $\text{Na}^+$  and  $\text{NO}_3^-$  did not affect the degrading performance of  $\text{Ag}_3\text{PO}_4@\text{MWCNTs@PANI}$  composite. However, phenol degradation efficiencies significantly decreased in the presence of  $\text{Na}_2\text{CO}_3$  and  $\text{NaCl}$ . To make a deep insight into the influence of inorganic ions on photocatalytic degradation rate, the corresponding pseudo-first-order kinetics curves were provided. As shown in Fig. 12b, in the presence of  $\text{CO}_3^{2-}$  and  $\text{Cl}^-$ , the apparent kinetic constants were  $0.13 \text{ min}^{-1}$  and  $0.018 \text{ min}^{-1}$ , respectively. Compared to the kinetic constants ( $0.35 \text{ min}^{-1}$ ) without ions addition, the rate constants were decreased by 62.9% and 94.9%, respectively, indicating that the reaction rate was also obviously suppressed in the presence of  $\text{CO}_3^{2-}$  and

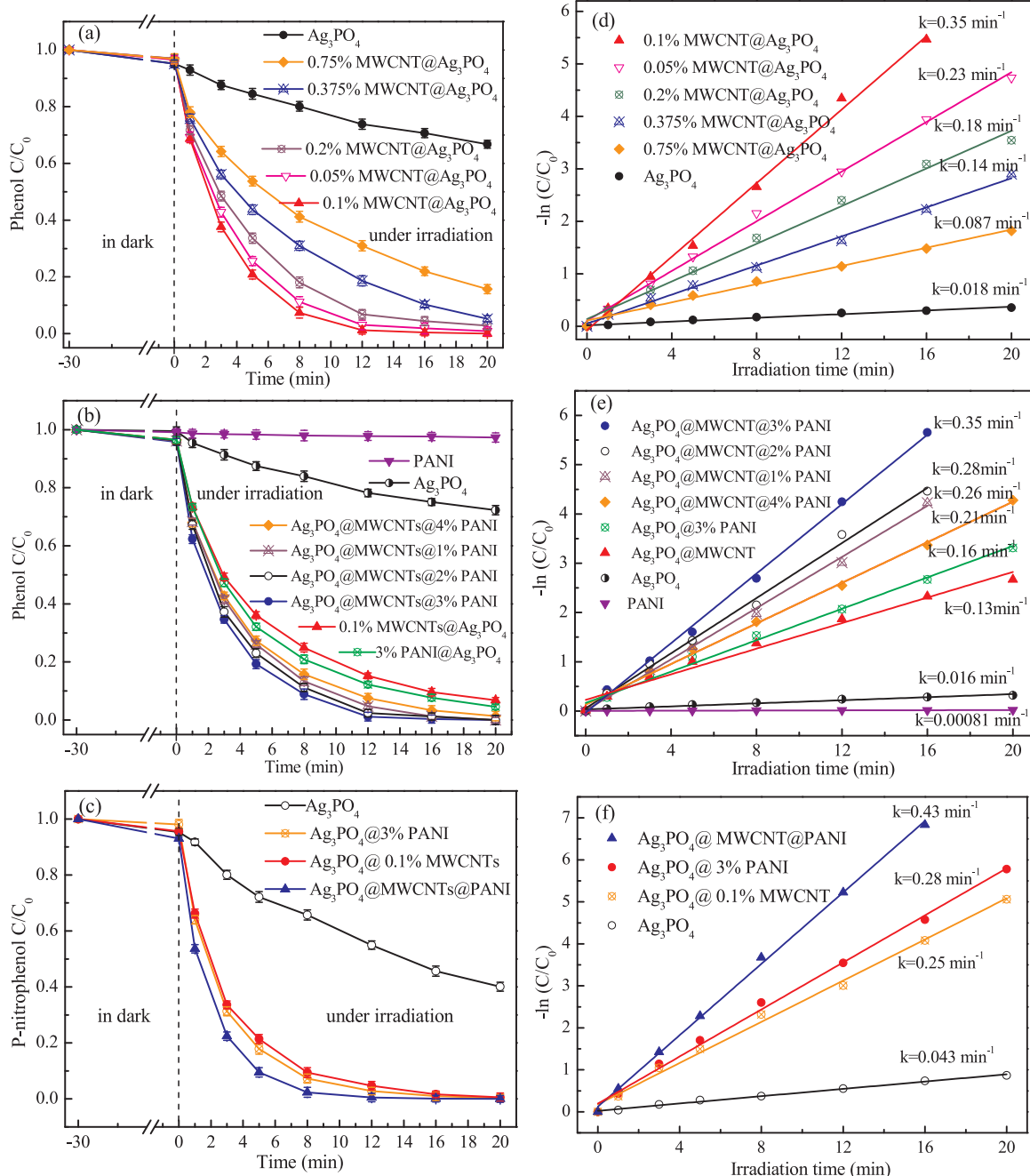


**Fig. 9.** Photodegradation curves of phenol (a) ([Phenol]: 20 mg L<sup>-1</sup>), (b) ([Phenol]: 25 mg L<sup>-1</sup>); Photodegradation curves of p-nitrophenol in the presence of as-prepared samples (c) ([p-nitrophenol]: 20 mg L<sup>-1</sup>); Reaction kinetic curves (d,e,f) of as-prepared samples corresponding to the photodegradation curves (a,b,c), respectively.

Cl-. In order to further explain these phenomena, the photocatalysts Ag<sub>3</sub>PO<sub>4</sub>@MWCNTs@PANI after reaction were collected and characterized by XRD, and the results were presented in Fig. S4. It can be seen that the diffraction peaks of Ag<sub>3</sub>PO<sub>4</sub>@MWCNTs@PANI cannot be observed, and instead the characteristic peak of AgCl (JCPDS No. 31-1238) appeared with the addition of NaCl, indicating that the crystal structure of Ag<sub>3</sub>PO<sub>4</sub>@MWCNTs@PANI was completely destroyed and transformed into AgCl. And partial AgCl was converted to metallic Ag (JCPDS No. 04-0783) after the light irradiation. Therefore, photocatalytic activity was significantly reduced because of the seriously destroyed Ag<sub>3</sub>PO<sub>4</sub> crystal structure [9]. From Fig. S4b it can be seen that Ag<sub>3</sub>PO<sub>4</sub>@MWCNTs@PANI was partially converted to Ag (JCPDS No. 04-0783), Ag<sub>2</sub>O (JCPDS No. 43-0997) and AgCl during

photodegradation in the presence of Na<sub>2</sub>CO<sub>3</sub>. A small amount of AgCl was detected because the Na<sub>2</sub>CO<sub>3</sub> used in this experiment is analytically pure, which contains impurity chlorine. The amount of impurity chlorine in high concentration of Na<sub>2</sub>CO<sub>3</sub> (0.1 mol/L) cannot be neglected, thus it was inevitably converted into a small amount of AgCl during the reaction. Moreover, CO<sub>3</sub><sup>2-</sup> was the scavengers of the hydroxyl radicals [46,50], which also caused a reduction in photocatalytic performance. The effect of pH values on the phenol degradation was presented in Fig. 12c, when the pH values were within the range of 5–11, the Ag<sub>3</sub>PO<sub>4</sub>@MWCNTs@PANI composite all displayed high photocatalytic activity towards phenol degradation, while the reduced photocatalytic activity at the pH values of 3.01 was observed. Previous studies have demonstrated that too low pH value may lead to changes

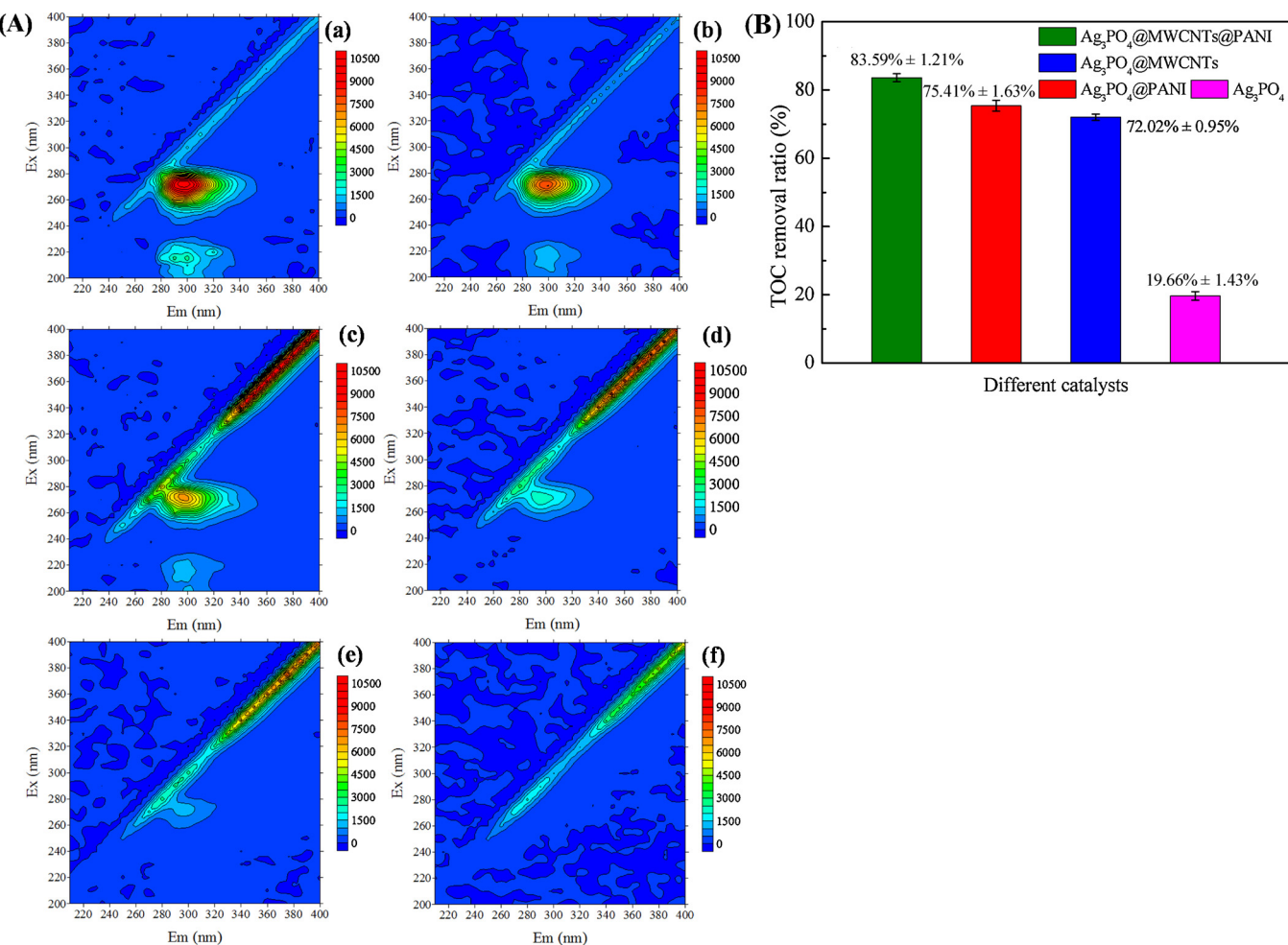


**Fig. 10.** (A) 3D EEMs of the phenol aqueous solution: (a) collected after 30 min adsorption in dark and (b–f) obtained after an irradiation time of 1, 3, 5, 8 and 20 min, respectively; (B) TOC removal of phenol over various photocatalysts under visible light irradiation for 20 min.

in Zeta potential of catalysts, which could affect the adsorption behavior of pollutants on the catalyst and the formation of free radicals during photocatalytic reaction [8,51–54]. So the Zeta potentials of  $\text{Ag}_3\text{PO}_4@\text{MWCNTs@PANI}$  at different pH conditions were measured, and the data were presented in Table S2. When the pH is in the range of 5–11, the absolute value of the Zeta potential was greater than 50 mV, which indicated the dispersion system with excellent stability. However, the Zeta potential changed drastically to  $-13.3 \text{ mV}$  at pH value of 3.02, which implied that properties of the photocatalyst were changed, and the dispersion system became unstable [55–57]. Hence, an unsatisfactory photocatalytic resulted from the changes of Zeta potential at acidic condition, which could impose adverse effect on the adsorption ability of photocatalyst and the formation of hydroxyl radicals, thus reducing the photocatalytic activity of the catalyst. Therefore, moderate pretreatment was necessary when the catalyst was used to treat the wastewater with low pH or carbonate and chloride anions. Despite this flaw, the relatively high performance was still obtained, suggesting that  $\text{Ag}_3\text{PO}_4@\text{MWCNTs@PANI}$  could work as an efficient photocatalyst for practical application in wastewater treatment.

### 3.5. Possible photocatalytic mechanism of $\text{Ag}_3\text{PO}_4@\text{MWCNTs@PANI}$

In order to investigate the main active species during the degradation process of phenol using the  $\text{Ag}_3\text{PO}_4@\text{MWCNTs@PANI}$  composite, the trapping experiments were carried out. The benzoquinone (BQ) was used as superoxide radical species ( $\cdot\text{O}_2^-$ ) scavenger, and ethylenediamine tetra acetic acid disodium salt (EDTA-2Na) as the hole ( $\text{h}^+$ )

scavengers. Isopropanol (IPA) and  $\text{AgNO}_3$  were employed as the scavengers of hydroxyl radical ( $\cdot\text{OH}$ ) and photogenerated electron ( $e^-$ ), respectively. As shown in Fig. 13a, the addition of BQ or EDTA-2Na led to a significant reduction in phenol degradation efficiency, especially in the presence of EDTA-2Na, resulting in almost complete deactivation of the  $\text{Ag}_3\text{PO}_4@\text{MWCNTs@PANI}$  photocatalyst. And the corresponding apparent rate constant declined from  $0.35 \text{ min}^{-1}$  to  $0.00015 \text{ min}^{-1}$ , which decreased by 99.96%. In the presence of BQ, the apparent rate constant dropped from  $0.35 \text{ min}^{-1}$  to  $0.016 \text{ min}^{-1}$ , leaving the decrease by 95.43% (Fig. 13b). The results indicated that the photogenerated hole ( $\text{h}^+$ ) and superoxide radical ( $\cdot\text{O}_2^-$ ) played an important role in the degradation of pollutants. Relatively obvious reduction of photocatalytic efficiency was also observed after the addition of  $\text{AgNO}_3$ , suggesting that the role of photogenerated electrons also cannot be ignored. Compared with the above quenchers, IPA had little effect on photocatalytic efficiency, but the rate constant decreased by 42.86%, indicating that some  $\cdot\text{OH}$  were also involved in the reaction procedure. The trapping experiments implied that  $\cdot\text{O}_2^-$ ,  $e^-$ ,  $\text{h}^+$  and  $\cdot\text{OH}$  all worked in the degradation process, while the major active species for the catalyst should be  $\text{h}^+$  and  $\cdot\text{O}_2^-$ , and phenol was mainly oxidized by holes directly. To further identify the radical generation in the photocatalytic system, the ESR spin-trap with DMPO technique was also performed. As presented in Fig. 13c and d, no signal of DMPO- $\cdot\text{O}_2^-$  and DMPO- $\cdot\text{OH}$  could be detected in the dark, proving  $\cdot\text{O}_2^-$  and  $\cdot\text{OH}$  radicals were generated during the photocatalytic reaction process. When exposed to the visible light, the characteristic signals of DMPO- $\cdot\text{O}_2^-$  and DMPO- $\cdot\text{OH}$  could be clearly observed, and the peaks intensity enhanced

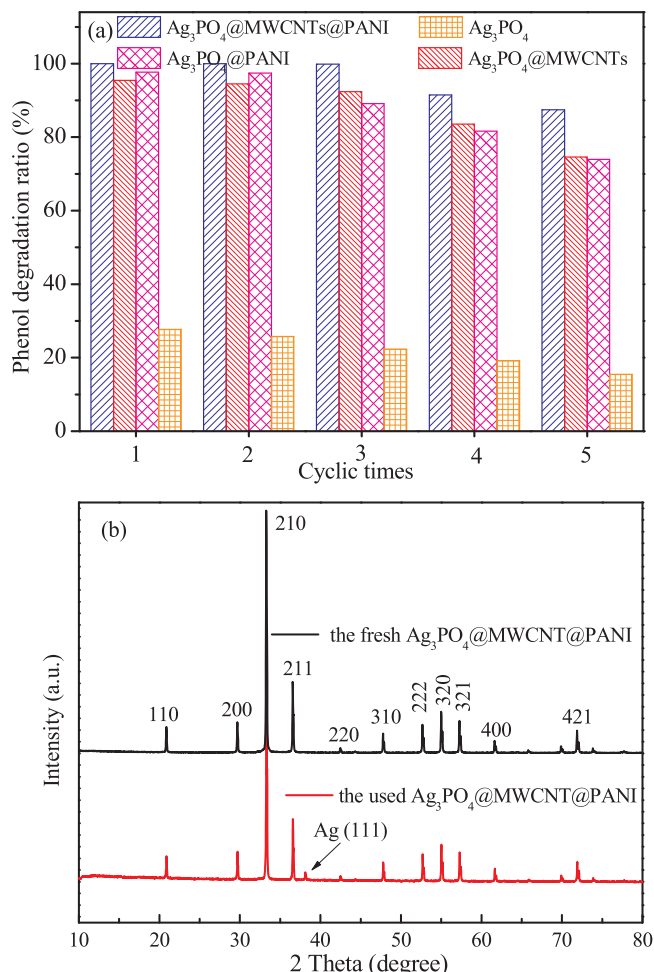


**Fig. 11.** Cycling test for the photocatalytic degradation of phenol (25 mg/L) in the presence of different as-prepared samples; (b) XRD patterns of the fresh and used  $\text{Ag}_3\text{PO}_4@\text{MWCNTs@PANI}$  composite.

obviously from the irradiation of 5 min to 10 min, further confirming that the  $\cdot\text{O}_2^-$  and  $\cdot\text{OH}$  radicals could be produced successfully on the surface of visible light-irradiated  $\text{Ag}_3\text{PO}_4@\text{MWCNTs@PANI}$  composite.

Based on the above experimental data and characteristic analysis, a possible photocatalytic mechanism of  $\text{Ag}_3\text{PO}_4@\text{MWCNTs@PANI}$  under visible light was proposed and briefly depicted in Scheme 1. According to the calculation results above, the conduction band potential ( $E_{\text{CB}}$ ) and valence band potential ( $E_{\text{VB}}$ ) of  $\text{Ag}_3\text{PO}_4$  were determined to be 0.43 eV and 2.69 eV, respectively. The LUMO and HOMO potentials of PANI were -2.1 and 1.3 eV, respectively [34,58,59]. Both  $\text{Ag}_3\text{PO}_4$  and PANI could be excited by visible light to produce photogenerated holes and excited electrons, respectively. The excited state electrons in PANI could readily inject into CB of  $\text{Ag}_3\text{PO}_4$ . It was well-known that PANI was an efficient conductive polymer with unique holes transporting properties [18–22]. For instance, Zhang et al. found that photo-generated holes in the VB of CdS could be transferred to the photocatalysts surface through HOMO of PANI [21]. The holes in VB of  $\text{TiO}_2$  can directly transfer to HOMO of PANI, and the photogenerated holes can emigrate to the photocatalysts surface easily [18]. And photo-generated holes in the ZnO valence band could transfer to the HOMO orbital of PANI and then emigrate to the photocatalysts surface and oxidize the adsorbed contaminants directly [22]. Therefore, PANI has been reported as a good material for transporting holes, which could separate the electron-hole pairs effectively and improve the photocatalytic ability remarkably. Similarly, the VB of  $\text{Ag}_3\text{PO}_4$  matches well with the HOMO of PANI. The photogenerated holes in the valence band

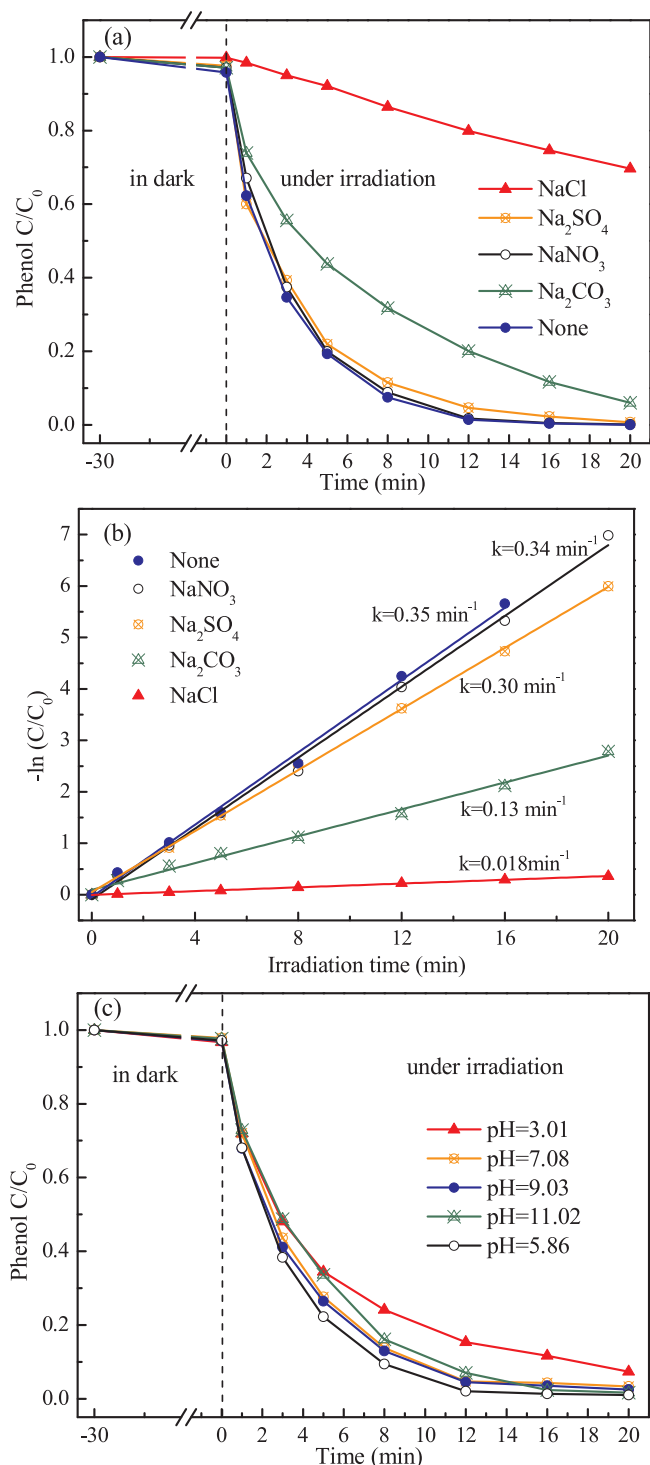


**Fig. 12.** Photodegradation curves of phenol with different inorganic salts (a) and corresponding reaction kinetic curves (b); (c) Photodegradation curves of phenol at different pH condition.

of  $\text{Ag}_3\text{PO}_4$  could be transferred quickly to the photocatalysts surface through the HOMO of PANI, with the effect of the heterojunction electric field at the interface of  $\text{Ag}_3\text{PO}_4$  and PANI [4]. The valence band potential of  $\text{Ag}_3\text{PO}_4$  is 2.69 eV, indicating that the photogenerated holes of  $\text{Ag}_3\text{PO}_4$  possessed very strong oxidative ability. The holes that quickly transferred from the bulk phase of  $\text{Ag}_3\text{PO}_4$  to the photocatalysts surface could directly oxidize and degrade the pollutants, which was in good agreement with the results of radical trapping experiments. Meanwhile, the excellent electrical conductivity along the MWCNTs

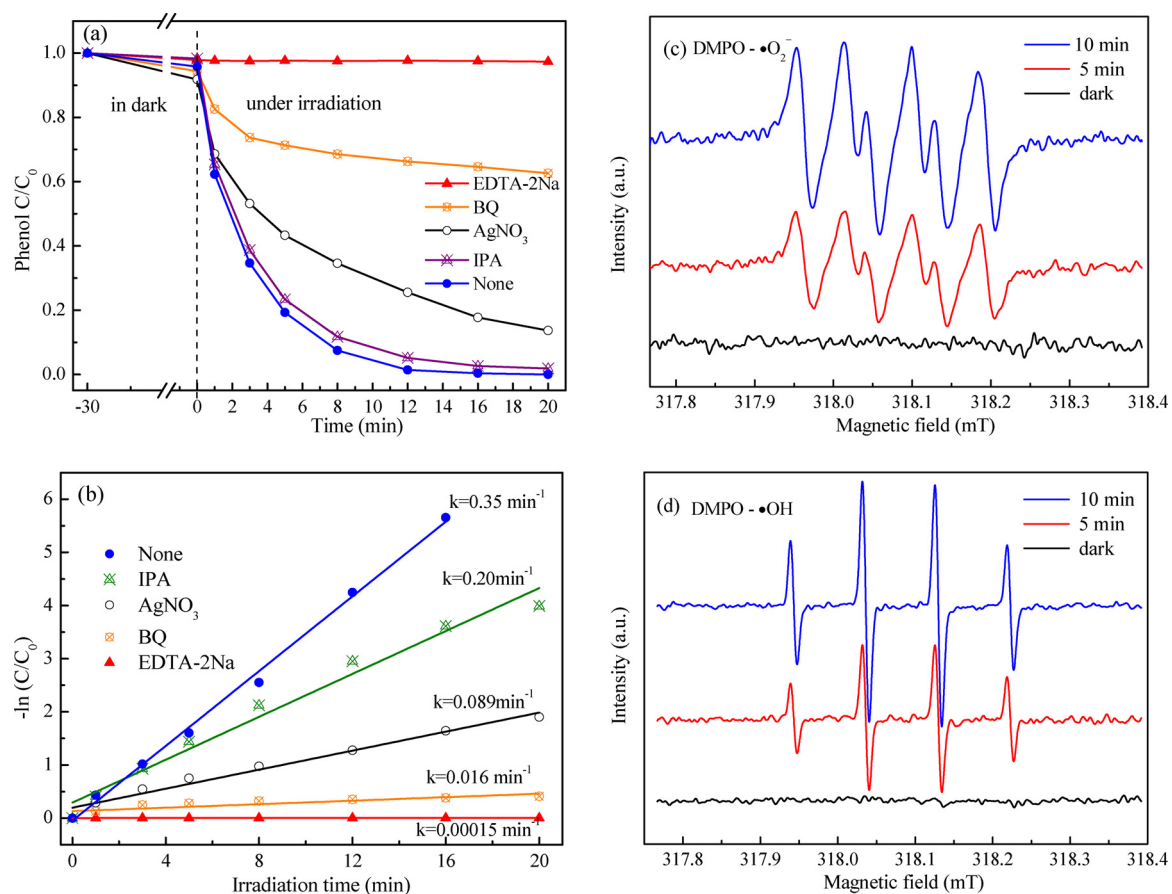
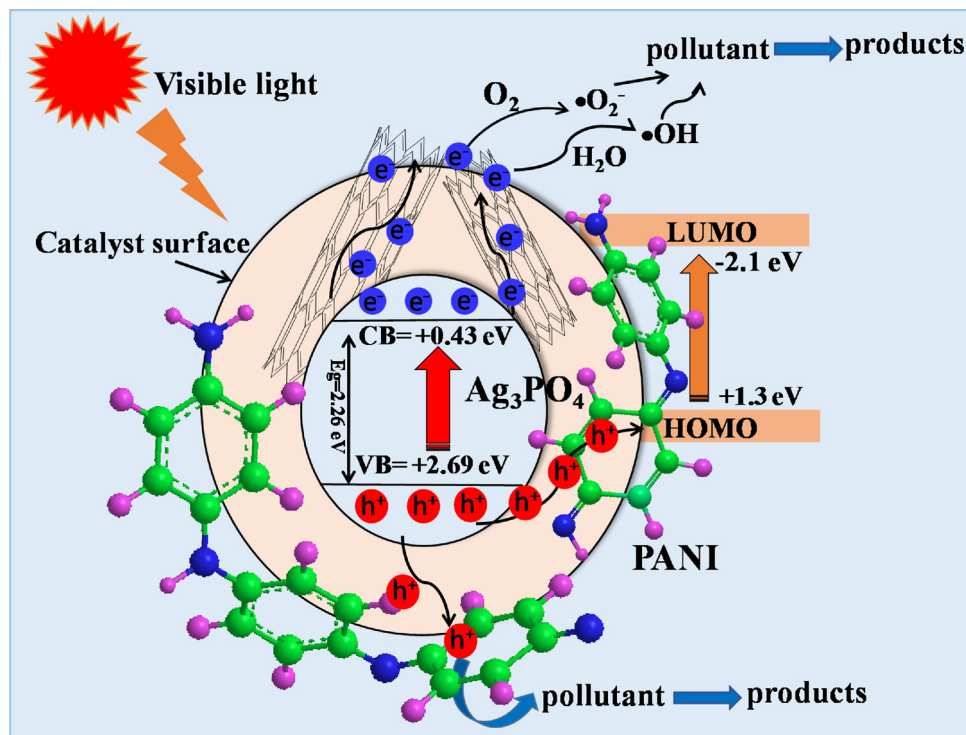


**Fig. 13.** Degradation curves of phenol with additions of scavengers under visible light over Ag<sub>3</sub>PO<sub>4</sub>@MWCNTs@PANI composite (a, degradation curve; b, corresponding reaction kinetic curves). DMPO spin-trapping ESR spectra for Ag<sub>3</sub>PO<sub>4</sub>@MWCNTs@PANI dispersion in the dark and under visible light irradiation (irradiation time of 5 and 10 min): (c) in methanol dispersion for DMPO-·O<sub>2</sub><sup>-</sup>; and (d) in aqueous dispersion for DMPO-·OH.



**Scheme 1.** Schematic illustration of photocatalytic mechanism for Ag<sub>3</sub>PO<sub>4</sub>@MWCNTs@PANI composite under visible light irradiation.

made it an effective acceptor and conductor of the photogenerated electrons [8,16,17,24]. MWCNTs have superior electronic properties such as large electron storage, which could as good electron acceptor and hence suppress recombination of the charge carriers [16]. Cai et. al [17] have reported that due to the good conductivity of MWCNTs, the electrons in the CB of  $\text{WO}_3$  and  $\text{Ag}_3\text{PO}_4$  could also be easily transferred to the surface of MWCNTs to participate in the photocatalytic reaction. In this study, the MWCNTs penetrating and doping in the bulk phase of  $\text{Ag}_3\text{PO}_4$  also could serve as conductors of photogenerated electrons and rapidly migrate electrons to the surface of the photocatalysts, and subsequently reacted with water and oxygen to yield hydroxyl and superoxide radicals, which would oxidize the organic pollutants. In addition, the rapid transportation and mobility of electrons on MWCNTs efficiently kept electrons away from the photogenerated holes, which could significantly promote the separation of photogenerated carriers and thus enhance the photocatalytic activity. In summary, based on the synergistic effect of the MWCNTs and PANI on  $\text{Ag}_3\text{PO}_4$ , the efficient charge separation and much lower charge recombination came true, and much smaller  $\text{Ag}_3\text{PO}_4$  crystals were also successfully prepared. The visible photocatalytic activities and photostability of  $\text{Ag}_3\text{PO}_4@\text{MWCNTs@PANI}$  photocatalysts were thus remarkably enhanced.

#### 4. Conclusions

In summary, a novel type of photocatalyst  $\text{Ag}_3\text{PO}_4@\text{MWCNTs@PANI}$  was synthesized successfully for the first time. The results of this study indicated that after the introduction of MWCNTs and PANI, the pure  $\text{Ag}_3\text{PO}_4$  with a diameter of about  $10\text{--}20\ \mu\text{m}$  were all changed into crystal particles with a diameter of  $0.38\text{--}1.0\ \mu\text{m}$  and  $0.15\text{--}0.38\ \mu\text{m}$ , respectively. The addition of MWCNTs and PANI significantly improved the visible light photocatalytic activity and photostability of the  $\text{Ag}_3\text{PO}_4$  photocatalyst. The photocatalytic activities for degradation of phenol and p-nitrophenol over  $\text{Ag}_3\text{PO}_4@0.1\%\text{MWCNTs@3\%PANI}$  composite both reached 100% in 20 min, the apparent rate constant of which was 21.9 and 10 times than that of the pure  $\text{Ag}_3\text{PO}_4$ , respectively. The radical trapping experiments and ESR analysis indicated that  $\cdot\text{O}_2^-$  and  $\text{h}^+$  played an important role during the photocatalytic degradation. The TOC removal efficiency of phenol reached 83.59% within the irradiation time of 20 min, suggesting good mineralization ability of the photocatalyst. The enhancement of photocatalytic activity and photostability were mainly attributed to the synergistic effect between MWCNTs and PANI on  $\text{Ag}_3\text{PO}_4$ . In this system, MWCNTs were utilized as the photogenerated electron conductors and PANI as the hole-transporting material, a rapid charge separation and slow charger combination thus came true. This work provides a promising and highly effective photocatalytic material having good potential of practical applications for environmental purification. The discovery of changes in crystal structure and properties of  $\text{Ag}_3\text{PO}_4$  due to the addition of MWCNTs and PANI, and synergistic effect among them offered a new strategy for preparing low-cost and efficient visible light active photocatalysts.

#### Acknowledgments

This work was supported by the project of National Natural Science Foundation of China (Grant No.: 51478172, 51278464, 51508538, and 51521006), the Natural Science Foundation of Zhejiang Province of China (Grant No.: LY17E080002) and the Department of Science and Technology of Hunan Province of China (Contract No.: 2017JJ2029 and 2017SK2362).

#### Appendix A. Supplementary data

Supplementary material related to this article can be found, in the online version, at doi:<https://doi.org/10.1016/j.apcatb.2018.12.048>.

#### References

- [1] J.A. Terrett, J.D. Cuthbertson, V.W. Shurtliff, D.W. Macmillan, Switching on elusive organometallic mechanisms with photoredox catalysis, *Nature* 524 (2015) 330–334.
- [2] K. Mori, K. Miyawaki, H. Yamashita, Ru and Ru-Ni nanoparticles on  $\text{TiO}_2$  support as extremely active catalysts for hydrogen production from Ammonia-Borane, *ACS Catal.* 6 (2016) 3128–3135.
- [3] Y. Bi, S. Ouyang, N. Umezawa, J. Cao, J.H. Ye, Facet effect of single-crystalline  $\text{Ag}_3\text{PO}_4$  sub-microcrystals on photocatalytic properties, *J. Am. Chem. Soc.* 133 (2011) 6490–6492.
- [4] Y.Y. Bu, Z.Y. Chen, Role of polyaniline on the photocatalytic degradation and stability performance of the polyaniline/silver/silver phosphate composite under visible light, *ACS Appl. Mater. Interfaces* 6 (2014) 17589–17598.
- [5] D.J. Martin, N. Umezawa, X.W. Chen, J.H. Ye, J.W. Tang, Facet engineered  $\text{Ag}_3\text{PO}_4$  for efficient water photooxidation, *Energy Environ. Sci.* 6 (2013) 3380–3386.
- [6] Y.P. Bi, H.Y. Hu, S.X. Ouyang, G.X. Lu, J.Y. Cao, J.H. Ye, Photocatalytic and photoelectric properties of cubic  $\text{Ag}_3\text{PO}_4$  sub-microcrystals with sharp corners and edges, *Chem. Commun.* 48 (2012) 3748–3750.
- [7] X.F. Yang, H.Y. Cui, Y. Li, J. Qin, R. Zhang, H. Tang, Fabrication of  $\text{Ag}_3\text{PO}_4$ -graphene composites with highly efficient and stable visible light photocatalytic performance, *ACS Catal.* 3 (2013) 363–369.
- [8] Y. Lin, S.H. Wu, X. Li, X. Wu, C.P. Yang, G.M. Zeng, Y.R. Peng, Q. Zhou, L. Lu, Microstructure and performance of Z-scheme photocatalyst of silver phosphate modified by MWCNTs and Cr-doped  $\text{SrTiO}_3$  for malachite green degradation, *Appl. Catal. B: Environ.* 227 (2018) 557–570.
- [9] T. Cai, Y.T. Liu, L.L. Wang, S.Q. Zhang, Y.X. Zeng, J.L. Yuan, J.H. Ma, W.Y. Dong, C.B. Liu, S.L. Luo, Silver phosphate-based Z-scheme photocatalytic system with superior sunlight photocatalytic activities and anti-photocorrosion performance, *Appl. Catal. B: Environ.* 208 (2017) 1–13.
- [10] Y. Bi, S. Ouyang, J. Cao, J.H. Ye, Facile synthesis of rhombic dodecahedral  $\text{AgX}/\text{Ag}_3\text{PO}_4$  ( $X = \text{Cl}, \text{Br}, \text{I}$ ) heterocrystals with enhanced photocatalytic properties and stabilities, *Phys. Chem. Chem. Phys.* 13 (2011) 10071–10075.
- [11] Y.Y. Bu, Z.Y. Chen, C.J. Sun, Highly efficient Z-Scheme  $\text{Ag}_3\text{PO}_4/\text{Ag}/\text{WO}_{3-x}$  photocatalyst for its enhanced photocatalytic performance, *Appl. Catal. B: Environ.* 179 (2015) 363–371.
- [12] C.F. Mu, Y. Zhang, W.Q. Cui, Y.H. Liang, Y.F. Zhu, Removal of bisphenol A over separation free 3D  $\text{Ag}_3\text{PO}_4$ -graphene hydrogel via an adsorption-photocatalysis synergy, *Appl. Catal. B: Environ.* 212 (2017) 41–49.
- [13] Y.P. Liu, L. Fang, H.D. Lu, L.J. Liu, H. Wang, C.Z. Hu, Highly efficient and stable  $\text{Ag}/\text{Ag}_3\text{PO}_4$  plasmonic photocatalyst in visible light, *Catal. Commun.* 17 (2012) 200–204.
- [14] Z.Y. Bai, Q. Yang, J.L. Wang, Catalytic ozonation of dimethyl phthalate using  $\text{Fe}_3\text{O}_4$ /multi-wall carbon nanotubes, *Environ. Technol.* 38 (2016) 2048–2057.
- [15] Y. Liu, Q. Fan, J.L. Wang, Zn-Fe-CNTs catalytic *in situ* generation of  $\text{H}_2\text{O}_2$  for Fenton-like degradation of sulfamethoxazole, *J. Hazard. Mater.* 342 (2017) 166–176.
- [16] P.N. Zhu, A.S. Nair, S.Y. Yang, S. Ramakrishna,  $\text{TiO}_2$ -MWCNT rice grain-shaped nanocomposites-synthesis, characterization and photocatalysis, *Mater. Res. Bull.* 46 (2012) 588–595.
- [17] L. Cai, X.L. Xiong, N.G. Liang, Q.Y. Long, Highly effective and stable  $\text{Ag}_3\text{PO}_4/\text{WO}_3/\text{MWCNTs}$  photocatalysts for simultaneous Cr(VI) reduction and orange II degradation under visible light irradiation, *Appl. Surf. Sci.* 353 (2015) 939–948.
- [18] H. Zhang, R.L. Zong, J.C. Zhao, Y.F. Zhu, Dramatic visible photocatalytic degradation performances due to synergistic effect of  $\text{TiO}_2$  with PANI, *Environ. Sci. Technol.* 42 (2008) 3803–3807.
- [19] Y.J. Wang, J. Xu, W.Z. Zong, Y.F. Zhu, Enhancement of photoelectric catalytic activity of  $\text{TiO}_2$  film via Polyaniline hybridization, *J. Solid State Chem.* 184 (2011) 1433–1438.
- [20] W.J. Jiang, W.J. Luo, R.L. Zong, W.Q. Yao, Z.P. Li, Y.F. Zhu, Polyaniline/carbon nitride nanosheets composite hydrogel: A separation-free and high-efficient photocatalyst with 3D hierarchical structure, *Small* 12 (2016) 4370–4378.
- [21] H. Zhang, Y.F. Zhu, Significant visible photoactivity and antiphotocorrosion performance of CdS photocatalysts after monolayer polyaniline hybridization, *J. Phys. Chem. C* 114 (2010) 5822–5826.
- [22] H. Zhang, R.L. Zong, Y.F. Zhu, Photocorrosion inhibition and photoactivity enhancement for Zinc oxide via hybridization with monolayer polyaniline, *J. Phys. Chem. C* 113 (2014) 4605–4611.
- [23] G. Bidan, E.M. Genies, M. Lapkowski, Polypyrrole and poly(N-methylpyrrole) films doped with Keggins-type heteropolyanions: preparation and properties, *J. Electroanal. Chem.* 251 (1988) 297–306.
- [24] B. Liu, Z.Y. Li, S. Xu, D.D. Han, D.Y. Lu, Enhanced visible-light photocatalytic activities of  $\text{Ag}_3\text{PO}_4/\text{MWCNT}$  nanocomposites fabricated by facile *in situ* precipitation method, *J. Alloys. Compd.* 596 (2014) 19–24.
- [25] C.Y. Feng, Y.C. Deng, L. Tang, G.M. Zeng, J.J. Wang, J.F. Yu, Y. Liu, B. Peng, H.P. Feng, J.J. Wang, Core-shell  $\text{Ag}_3\text{CrO}_4/\text{N-GQDs@g-C}_3\text{N}_4$  composites with anti-photocorrosion performance for enhanced full-spectrum-light photocatalytic activities, *Appl. Catal. B: Environ.* 239 (2018) 525–536.
- [26] L. Lu, Y. Lin, Q.W. Chai, S.Y. He, C.P. Yang, Removal of acenaphthene by biochar and raw biomass with coexisting heavy metal and phenanthrene, *Colloids Surf. A Physicochem. Eng. Asp.* 558 (2018) 103–109.
- [27] J. Li, S.B. Tang, L. Lu, H.C. Zeng, Preparation of nanocomposites of metals, metal Oxides, and carbon nanotubes via self-assembly, *J. Am. Chem. Soc.* 129 (2007) 9401–9409.
- [28] J.D. Wang, J.K. Liu, C.X. Luo, Y. Lu, X.H. Yang, Silver phosphate crystal growth by

- screw dislocation driven of dynamic-template, *Cryst. Growth Des.* 13 (2013) 4837–4843.
- [29] I. Karatchevtseva, Z.M. Zhang, J. Hanna, V. Luca, Electrosynthesis of macroporous polyaniline-V<sub>2</sub>O<sub>5</sub> nanocomposites and their unusual magnetic properties, *Chem. Mater.* 18 (2006) 4908–4916.
- [30] D.P. Wang, H.C. Zeng, Nanocomposites of anatase-polyaniline prepared via self-assembly, *J. Phys. Chem. C* 113 (2009) 8097–8106.
- [31] L. Tang, C.Y. Feng, Y.C. Deng, G.M. Zeng, J.J. Wang, Y.N. Liu, H.P. Feng, J.J. Wang, Enhanced photocatalytic activity of ternary Ag/g-C<sub>3</sub>N<sub>4</sub>/NaTaO<sub>3</sub> photocatalysts under wide spectrum light radiation: the high potential band protection mechanism, *Appl. Catal. B: Environ.* 230 (2018) 102–114.
- [32] Y. Matsumoto, Energy positions of oxide semiconductors and photocatalysis with iron complex oxides, *J. Solid State Chem.* 126 (1996) 227–234.
- [33] P.Y. Dong, Y.H. Wang, B.C. Cao, S.Y. Xin, L.N. Guo, J. Zhang, F.H. Li, Ag<sub>3</sub>PO<sub>4</sub>/reduced graphite oxide sheets nanocomposites with highly enhanced visible light photocatalytic activity and stability, *Appl. Catal. B: Environ.* 132–133 (2013) 45–53.
- [34] L. Liu, L. Ding, Y.G. Liu, W.J. An, S.L. Lin, Y.H. Liang, W.Q. Cui, A stable Ag<sub>3</sub>PO<sub>4</sub>@PANI core@shell hybrid: enrichment photocatalytic degradation with π-π conjugation, *Appl. Catal. B: Environ.* 201 (2016) 92–104.
- [35] C.P. Yang, H. Chen, G.M. Zeng, G.L. Yu, S.L. Luo, Biomass accumulation and control strategies in gas biofiltration, *Biotechnol. Adv.* 28 (2010) 531–540.
- [36] Z. Wang, Y. Lu, M. Zhang, G.W. Zhou, H. Fei, H.X. Shi, H.J. Dai, Synthesis and characterization of Ag<sub>3</sub>PO<sub>4</sub>/multiwalled carbon nanotube compositephotocatalyst with enhanced photocatalytic activity and stability under visible light, *J. Mater. Sci.* 49 (2014) 1585–1593.
- [37] A. Amiri, M. Shanbedi, H. Eshghi, S.Z. Heris, M. Baniadam, Highly dispersed multiwalled carbon nanotubes decorated with Ag nanoparticles in water and experimental investigation of the thermophysical properties, *J. Phys. Chem. C* 116 (2012) 3369–3375.
- [38] Y. Cheng, H.J. He, C.P. Yang, G.M. Zeng, X. Li, H. Chen, G.L. Yu, Challenges and solutions for biofiltration of hydrophobic volatile organic compounds, *Biotechnol. Adv.* 34 (2016) 1091–1102.
- [39] F. Chen, Q. Yang, J. Sun, F.B. Yao, S. Wang, Y.L. Wang, X.L. Wang, X.M. Li, C.G. Niu, D.B. Wang, G.M. Zeng, Enhanced photocatalytic degradation of tetracycline by AgI/BiVO<sub>4</sub>heterojunction under visible-light irradiation: mineralization efficiency and mechanism, *ACS Appl. Mater. Interfaces* 8 (2016) 32887–32900.
- [40] Q. Zhou, Y. Lin, X. Li, C.P. Yang, Z.F. Han, G.M. Zeng, L. Lu, S.Y. He, Effect of zinc ions on nutrient removal and growth of *Lemna aquinoctialis* from anaerobically digested swine wastewater, *Bioresour. Technol.* 249 (2017) 457–463.
- [41] X.J. Chen, Y.Z. Dai, X.Y. Wang, Methods and mechanism for improvement of photocatalytic activity and stability of Ag<sub>3</sub>PO<sub>4</sub>: a review, *J. Alloys. Compd.* 649 (2015) 910–932.
- [42] H. Guo, C.G. Niu, L. Zhang, X.J. Wen, C. Liang, X.G. Zhang, D.L. Guan, N. Tang, G.M. Zeng, Construction of direct Z-scheme AgI/Bi<sub>2</sub>Sn<sub>2</sub>O<sub>7</sub> nanojunction system with enhanced photocatalytic activity: accelerated interfacial charge transfer induced efficient Cr(VI) reduction, tetracycline degradation and *Escherichia coli* inactivation, *ACS Sustain. Chem. Eng.* 6 (2018) 8003–8018.
- [43] K. Awazu, M. Fujimaki, C. Rockstuhl, J. Tominaga, H. Murakami, Y. Ohki, N. Yoshida, T. Watanabe, A plasmonic photocatalyst consisting of silver nanoparticles embedded in titanium dioxide, *J. Am. Chem. Soc.* 130 (2008) 1676–1680.
- [44] Y. Yang, Z.T. Zeng, C. Zhang, D.L. Huang, G.M. Zeng, R. Xiao, C. Lai, C.Y. Zhou, H. Guo, W.J. Xue, M. Cheng, W.J. Wang, J.J. Wang, Construction of iodine vacancy-rich BiOI/Ag@AgI Z-scheme heterojunction photocatalysts for visible-light-driven tetracycline degradation: transformation pathways and mechanism insight, *Chem. Eng. J.* 349 (2018) 808–821.
- [45] Y.P. Liu, F. Liang, H.D. Lu, Y.W. Li, C.Z. Hu, H.G. Yu, One-pot pyridine-assisted synthesis of visible-light-driven photocatalyst Ag/Ag<sub>3</sub>PO<sub>4</sub>, *Appl. Catal. B: Environ.* 115–116 (2012) 245–252.
- [46] Y.F. Wang, X.L. Wang, H. Li, K.F. Lin, P. Wang, J. Yang, Y.D. Liu, Z.Y. Sun, L.H. Fan, Z.M. Wu, Treatment of high salinity phenol-laden wastewater using a sequencing batch reactor containing halophilic bacterial community, *Int. Biodeterior. Biodegr.* 93 (2014) 138–144.
- [47] X.X. Cheng, R.F. Chong, Y.Y. Cao, D.L. Li, Z.X. Chang, L. Zhang, Influence of inorganic anions on photocatalytic degeneration of methylene blue on Ag<sub>3</sub>PO<sub>4</sub>, *J. Nanosci. Nanotechnol.* 16 (2016) 12489–12497.
- [48] H.J. He, Y.J. Chen, X. Li, Y. Cheng, C.P. Yang, G.M. Zeng, Influence of salinity on microorganisms in activated sludge processes: a review, *Int. Biodeterior. Biodegr.* 119 (2016) 520–527.
- [49] Y.J. Chen, H.J. He, H.Y. Liu, H.R. Li, G.M. Zeng, X. Xia, C.P. Yang, Effect of salinity on removal performance and activated sludge characteristics in sequencing batch reactors, *Bioresour. Technol.* 249 (2018) 890–899.
- [50] J.E. Grebel, J.J. Pignatello, W.A. Mitch, Effect of halide ions and carbonates on organic contaminant degradation by hydroxyl radical-based advanced oxidation processes in saline waters, *Environ. Sci. Technol.* 44 (2010) 6822–6828.
- [51] A. Machulek, J.E.F. Moraes, C. Vautiergiongo, C.A. Silverio, L.C. Friedrich, C.A.O. Nascimento, M.C. Gonzalez, F.H. Quina, Abatement of the inhibitory effect of chloride anions on the photo-fenton process, *Environ. Sci. Technol.* 41 (2007) 8459–8463.
- [52] H.J. He, Z.H. Xiang, X.J. Chen, H. Chen, H. Huang, M. Wen, C.P. Yang, Biosorption of Cd(II) from synthetic wastewater using dry biofilms from biotrickling filters, *Int. J. Environ. Sci. Technol.* 15 (2018) 1491–1500.
- [53] B. Samiey, A.R. Toosi, Adsorption of malachite green on silica gel: effects of NaCl, pH and 2-propanol, *J. Hazard. Mater.* 184 (2010) 739–745.
- [54] Q.W. Chai, L. Lu, Y. Lin, X.Q. Ji, C.P. Yang, S.Y. He, D. Zhang, Effects and mechanisms of anionic and nonionic surfactants on biochar removal of chromium, *Environ. Sci. Pollut. Res. Int.* 25 (2018) 18443–18450.
- [55] S.H. Wu, H.R. Li, X. Li, H.J. He, C.P. Yang, Performances and mechanisms of efficient degradation of atrazine using peroxymonosulfate and ferrate as oxidants, *Chem. Eng. J.* 353 (2018) 533–541.
- [56] L. Chen, C. Xu, J. Liu, X. Fang, Z. Zhang, Optical absorption property and photo-thermal conversion performance of graphene oxide/water nanofluids with excellent dispersion stability, *Sol. Energy* 148 (2017) 17–24.
- [57] S.H. Wu, H.J. He, X. Li, C.P. Yang, G.M. Zeng, B. Wu, S.Y. He, L. Lu, Performances and mechanisms of efficient degradation of atrazine using peroxymonosulfate and ferrate as oxidants, *Chem. Eng. J.* 341 (2018) 126–136.
- [58] F. Wang, S.X. Min, TiO<sub>2</sub>/polyaniline composites: an efficient photocatalyst for the degradation of methylene blue under natural light, *Chin. Chem. Lett.* 18 (2007) 1273–1277.
- [59] G.K.R. Senadeera, T. Kitamura, Y. Wada, S. Yanagida, Deposition of polyaniline via molecular self-assembly on TiO<sub>2</sub> and its uses as a sensitiser in solid-state solar cells, *J. Photochem. Photobiol. A: Chem.* 164 (2004) 61–66.